PHYSICAL REVIEW B VOLUME 43, NUMBER 4 1 FEBRUARY 1991

Micromagnetics of domain walls at surfaces

M. R. Scheinfein, J. Unguris, J. L. Blue, K. J. Coakley, D. T. Pierce, and R. J. Celotta
National Institute of Standards and Technology, Gaithersburg, Maryland 20899

P. J. Ryan
Seagate Technology, 7801 Computer Avenue, Bloomington, Minnesota 55435
(Received 25 July 1990; revised manuscript received 11 September 1990)

High-spatial-resolution magnetization maps of ferromagnetic surfaces are generated with use of scanning electron microscopy with polarization analysis (SEMPA). The structure of surface Néel walls is measured by SEMPA and compared directly to the results of micromagnetics simulations. We find that the surface magnetic properties observed with SEMPA can be modeled using standard micromagnetic theory using only bulk parameters. Surface-domain-wall magnetization profiles were measured, using two different probe diameters in each case, for an Fe(100) single crystal and for Permalloy films with thicknesses of 0.12, 0.16, 0.20, and 0.24 μm. In making the quantitative comparison to the surface-domain-wall profiles calculated from (bulk) micromagnetic theory, the rms deviations, the χ^2 statistic, a correlation statistic, and rms deviations at 5% and 95% confidence levels were determined for each case. The calculated and measured domain wall profiles agree on the average to within $\pm 7.8\%$ for 180° walls in semi-infinite crystals of Fe(100), and $\pm 4.5\%$ for 180° walls in thin films of Permalloy. The micromagnetic simulations show the 180° wall of the bulk turning over into a Néel wall at the surface with the magnetization in the plane of the surface. The Néel wall extends from the surface into the bulk over a depth approximately equal to a Bloch-wall width.

I. INTRODUCTION

The surface of a ferromagnetic material is important in defining equilibrium micromagnetic structure. Equilibrium configurations result from the minimization of energy through the formation of domains and domain walls.[1–32] Surface magnetic microstructure is important to the understanding of fundamental properties of magnetic materials as well as the limitations on the density of information stored on magnetic media. Although there has been intense research into the structure of domains and domain walls, in bulk and at surfaces, there has not been an experimental technique with which one can quantitatively observe detailed micromagnetic structure at submicrometer length scales for bulk ferromagnets. Transmission electron microscopy techniques have been used to study domain walls in thin films,[33–46] while domain-wall studies of bulk samples using optical[47–49] and Bitter techniques have limited spatial resolution.[50–52] Over the past few years, the technique of scanning electron microscopy with polarization analysis (SEMPA) has been developed as a means to obtain high-resolution quantitative maps of the surface magnetization for both thin-film and bulk samples. From such measurements, one can obtain the profile of the magnetization across a domain wall at its intersection with the surface.[53,54]

In a previous short paper,[54] hereafter referred to as I, we reported the first comparison between surface-domain-wall profiles, which we measured using SEMPA, and calculated profiles, which we obtained from a micromagnetic simulation. The present paper provides many of the details absent in the shorter paper and further extends and quantifies the analysis of the data. In I, surface-domain-wall profiles were extracted from SEMPA magnetization images of three materials: an Fe(100) single crystal, a Co-based ferromagnetic glass, and a Permalloy thin film. In lower-magnetocrystalline-anisotropy materials, a Bloch wall, a domain wall in which the magnetization rotates in the plane of the wall, does not terminate abruptly at the surface with magnetization exiting the surface; rather, the magnetization turns over and lies in the surface in one of the two directions perpendicular to the plane of the Bloch wall. These Néel-like walls at the surface avoid stray magnetic fields and thus minimize the magnetostatic energy.[11] Where two surface Néel walls which result from a single Bloch wall turning over in two opposite directions meet, there is an offset which was also measured using SEMPA. The measured magnetization profiles across surface Néel walls were found to be asymmetric.

We employed nonlinear micromagnetic equations to simulate the Bloch wall in the bulk and its intersection with the surface. Whereas the experiment probes only the near-surface region, the simulations give information on the bulk as well as the surface. The good agreement (reported in I and further supported and quantified in the present paper) between the micromagnetic simulations and the measured surface-Néel-wall profiles and offsets suggests that the calculations give reliable information about the bulk. The calculations show that the surface Néel wall is about twice as wide as the bulk Bloch wall. The micromagnetic simulations also show that the depth of the Néel-wall region at the surface is approximately

equal to the bulk Bloch-wall width. This is supported by the agreement we present in this paper comparing profiles of a surface Néel wall which was wide enough to be measured by the Kerr effect, which has a probing depth of about 15 nm, and by SEMPA, which has a probing depth of order 1 nm, both less than a typical Bloch-wall width.

One of the aims of the present paper is to quantify the comparison of the micromagnetic simulations and the measured surface-domain-wall profiles. This is of particular interest because the agreement between the measurements and calculations is obtained using only bulk parameters in the micromagnetic simulation. We will show that including surface anisotropy produces changes smaller than the experimental uncertainty. The effect of the surface on the domain wall occurs over a length scale characterized by the width of a Bloch wall in contrast to some other magnetic effects at surfaces which occur over much shorter length scales. We list three effects which occur over these short length scales. (1) The measured decrease with temperature in the magnetization at the surface[55,56] was interpreted[57,58] to be due to an exchange coupling of the outer surface layer to the bulk equal to only 0.3 of the bulk exchange. (2) The surface magnetization may have a different dependence on applied magnetic field (hysteresis curve).[59] (3) Magnetic moments at the surface are enhanced owing to the reduced coordination and narrowing of the d band.[60] These three effects occur at the outer atomic layer or two, in contrast to the relatively long length scale for changes in magnetic microstructure at the surface. Thus, even though SEMPA is surface sensitive, we are unlikely to obtain information on short-magnetic-length-scale phenomena by measuring domains and domain walls at surfaces, the energetics of which cause changes over a longer range.

In Sec. II we describe the SEMPA apparatus and measurement technique. A typical image for an Fe(100) surface of a single-crystal whisker is presented. A careful analysis is given of the probe-size and scan-length calibration. We describe the data processing and how the experimental uncertainty in the measurement of the domain-wall profile is determined.

In Sec. III we describe the magnetic microstructure simulations. The details of the calculations are given in this section and the Appendix. The sensitivity of the calculation to the geometrical and magnetic parameters is tested, and an upper limit on the uncertainty introduced on the results by possible variations of the parameters is thereby determined. By using periodic boundary conditions, it is possible to simulate an infinite crystal with uniaxial anisotropy and compare our result to the textbook result using a variational approach. For the infinite crystal with cubic anisotropy, we find that the 180° wall separates into two 90° walls. For a crystal with a surface, we find the magnetostatic energy at the surface is sufficient to force a 180° wall to form without introducing any effects due to magnetostriction. Explicit values of the wall energies are reported for different cases. Asymmetric Bloch walls are found in simulations for thin films.

In Sec. IV we present the experimental wall profiles and compare them to the results of the magnetic simulations. We present profiles from an Fe whisker measured with two different SEM probe sizes and for comparison show the domain-wall profile of Fe measured by Oepen and Kirschner.[53] We show our measurements for Permalloy films of four different thicknesses measured with different probe sizes. The data we show in this paper have a better signal-to-noise ratio than those previously presented in I. The surface-domain-wall profile of the Co-based ferromagnetic glass reported in I was erroneously compressed on the horizontal axis by a factor of 2 from the correct measured width. The parameters used in the simulation were later determined to be inappropriate.[61] There is some uncertainty in the correct value of the anisotropy to use for such a simulation. The measured macroscopic anisotropy may differ from the local anisotropy that determines the structure of the wall. Since neither the exchange nor the anisotropy parameters appropriate for a simulation are as well known in the case of the metallic glass as for Fe or Permalloy, we have omitted analysis of such materials in this paper. For the other materials a detailed statistical analysis is given of the fit of the model to the data. Both a χ^2 and an R^2 correlation analysis are calculated, and confidence intervals for each are determined.

Further discussion of our results and conclusions are summarized in Sec. V.

II. EXPERIMENT

The principle of scanning electron microscopy with polarization analysis (SEMPA) is illustrated schematically in Fig. 1. A finely focused beam of medium-energy (5–50 keV) unpolarized electrons is rastered across a sample's surface. Secondary electrons are excited near the surface by scattering of the primary electron beam. The secondary electrons emitted from the valence band of a ferromagnetic sample retain their spin orientation. The net polarization of the emitted secondary electrons is characteristic of the net spin density in the solid for a variety of ferromagnetic materials. Surface magnetization maps can be generated at high spatial resolution by spin

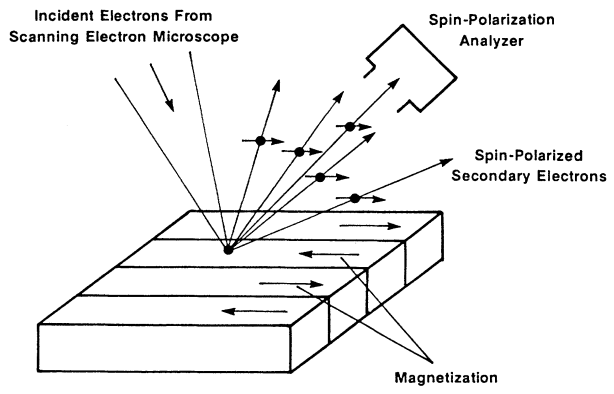

FIG. 1. Schematic representation of SEMPA. A focused beam of medium-energy electrons excites polarized secondary electrons in a ferromagnet. These electrons are subsequently spin analyzed.

analyzing the emitted secondary electrons, point by point, as the incident beam rasters the sample surface, as has been demonstrated by a number of groups.[53,54,62–64] The only significant constraints imposed on the sample are that it be conducting or semiconducting to prevent charging under the incident electron beam, and that the sample not possess large fringe fields which will depolarize the low-energy-polarized secondary electrons emitted from the sample surface. We have calculated the spin precession of electrons in the fringe fields of domain walls and found it to be negligible for all cases presented here.

As SEMPA is a surface-sensitive, magnetic-microstructural-analysis technique, the environment local to the sample surface must be ultrahigh vacuum (UHV). In our current implementation of SEMPA, we retrofited a high-resolution UHV Auger microprobe with low-energy diffuse scattering (LEDS) electron-spin polarization analyzers.[65,66] A complete description of our SEMPA apparatus has been published.[67,68]

The SEMPA mode of operation in our apparatus uses a 10-keV electron-beam energy, at a 10-mm working distance with extraction fields due to the SEMPA electron optics near the sample surface of 150 V/mm.[67] The specimen stage is tilted at 45° with respect to the incident-beam direction,[67] which elongates the probe in one direction. For measurement of the domain-wall profiles, we orient the domain walls so as to maximize the spatial resolution during a measurement. The scanned area on the sample was corrected to account for a sample tilt such that the magnification was equal in both scan directions. The SEMPA measurements of domain-wall profiles reported here were acquired at a linear magnification of 25 000×. All of the SEMPA images used for this study are comprised of 192×256 square picture elements (pixels). The dwell time per pixel was 30 ms, for a total image-acquisition time of 24.5 min. The two in-plane magnetization images, together with the standard secondary-intensity image, were acquired simultaneously and are therefore registered exactly.

SEMPA images of the x and y components of the surface magnetization from a region near a 180° surface domain wall in a single crystal of Fe(100) are shown in Figs. 2(a) and 2(b), respectively. These images are 3 μm across and were acquired with an incident-electron-beam current of 1.6 nA. Both SEMPA magnetization images show positive (negative) magnetization, $+M$ ($-M$), as white (black). In Fig. 2(a) the positive x component of the magnetization, M_x, points to the right, whereas in Fig. 2(b) the positive y component of the magnetization, M_y, points upward in the plane of the paper. Both M_x and M_y components of the magnetization are in the plane of the page. We measured no out-of-plane component of the magnetization M_z for this surface-domain wall structure, indicating that the magnetization lies in the plane of the surface even when the bulk Bloch wall in the interior of the film points normal to the surface. Figure 2(a) and 2(b) are representative of the SEMPA images from which we extract surface-domain-wall magnetization profiles. In Fig. 2(a) it is also evident that the direction of the domain wall changes near the center of image. This is a surface magnetic quasisingularity.[69] The surface walls

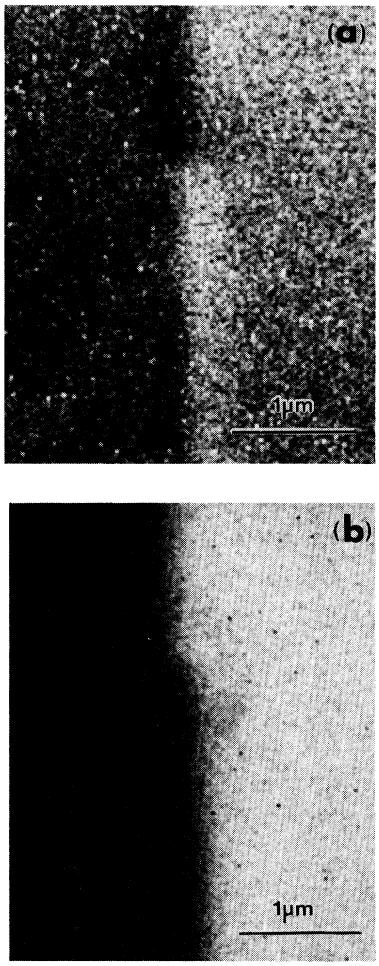

FIG. 2. (a) M_x and (b) M_y SEMPA images from the surface of a single crystal of Fe(100). The surface domain wall runs vertically through the image. In the center is a surface magnetic singularity about which the magnetization circulates.

are offset from each other on either side of the surface singularity.[54,70] This surface-domain-wall offset on either side of the surface singularity and the surface-domain-wall magnetization profiles will be used to test the results of micromagnetic theory.

A. SEMPA probe size and calibration

The spatial resolution for the determination of magnetic microstructure using SEMPA was limited by the size of the 10-keV focused electron beam incident on the sample and the interaction region for the production of secondaries which arrive at the spin detector. The mean penetration depth for 10-keV electrons in materials such as Fe is on the order of 1 μm.[17] The beam enters the sample surface with a width equal to the beam diameter and spreads as it penetrates deeper into the sample.[71] The spread of the incident electron beam within the sam-

ple is usually referred to as the "blooming" effect. If all of the secondary electrons which are created in the bloom escape from the sample surface and are detected by the spin analyzer, the spatial resolution of the technique is limited by the bloom diameter. Since we measured the spin polarization of secondary electrons with an energy between 0 and 10 eV (with respect to the vacuum level), we expect that the information depth for the SEMPA measurement was limited by the escape depth of these low-energy secondary electrons. Measurements of the escape depth of polarized secondary electrons that have been made indicate that the mean free path is on the order of a nanometer.[72] There remains some controversy about this, in part due to the material dependence of this quantity. Since the upper limit for the mean free path is on the order of nanometers and the probe diameter in our scanning Auger microprobe is on the order of tens of nanometers, the spatial resolution that we can achieve with our current apparatus is limited by the incident probe diameter. We infer this from geometrical considerations. The incident probe diameter is not significantly expanded by traversing several nanometers of material.[71] If the secondary electrons were emitted isotropically from a depth of several nanometers, the effective sampling region may be several nanometers larger than the incident probe diameter. This would produce only a small fractional change in the sampling region for a 70-nm-diam electron probe.

We note that secondary electrons are also produced by backscattered primary electrons from deep within the "bloom" in the bulk. These secondaries, called SE_2, are generally considered to be spatially distributed on the surface within a diameter equal to half of the range that the primary electrons penetrate the solid,[71] in our case a diameter of 0.5 μm. For transition metals it is believed that the total number of the secondaries produced by backscattered primaries, SE_2, is nearly equal to those produced by the incident beam.[71] In the experiments we will present on domain walls, the SE_2 electrons would sample a 0.5-μm-diam region of the surface magnetization. When the beam is centered on the wall, there would be a net decrease of up to 50% in the magnitude of the measured magnetization. As we do not observe this drastic decrease in magnetization near the wall, it appears that the effect of SE_2 electrons is small. We will study this in more detail in the future.

We have measured the probe diameter for our scanning Auger microprobe operated in the SEMPA mode. The incident-electron-beam distribution can be assessed from line-scan profiles across a cleaved GaAs crystal edge oriented normal to the beam-scan direction. The secondary-intensity images of the cleaved edges were acquired through the SEMPA transport optics. All possible beam-broadening effects such as those caused by mechanical or electrical instabilities were included. Crystals were selected with edges which were extremely thin and undercut. This together with the planar extraction fields in our apparatus prevented electrons from beneath the undercut edge from reaching the SEMPA detector.[67] The measured edge profiles were then a convolution of the beam profile with a step function, from which the edge profiles were differentiated to recover the probe shape.

Prior to measuring the probe profile, the length scale of the scans was calibrated by measuring the line spacing of a 0.46-μm diffraction grid as a function of the magnification. The absolute error in the length scale was less than 2.0%, and no magnification correction was made.

The probe size in an Auger microprobe depends on various electron-lens excitations and angular-limiting apertures in the electron optical column. Thus the probe size becomes a sensitive function of the current in the electron beam. In Figs. 3(a)–3(c) the measured probe-intensity distributions for the three sets of operating conditions used for the acquisition of the domain-wall data are shown. We identify the probe distribution by the current in the probe. The smallest probe in Fig. 3(a) has the smallest current, $I=0.3$ nA. The solid circles are the in-focus condition, and the open squares are the in-focus condition on the next day. This illustrates stability and reproducibility. As the operating conditions under which this profile was acquired were diffraction limited (in contrast to aberration limited), the probe-intensity distribution was insensitive to slight changes in the objective-(final-focusing) lens excitation. This is important because focusing on a perfect crystal surface can be difficult. The solid line in Fig. 3(a) is a fit to the probe distribution by a Gaussian. This Gaussian has a full width at half maximum (FWHM) of 0.070 μm. We will use this fit to the probe distribution to convolve the probe size with the calculated profiles in order to make a quantitative comparison of the micromagnetic theory to our domain-wall data. In Figs. 3(b) and 3(c) the probe-intensity distributions for incident-beam currents $I=0.6$ and 1.6 nA are shown respectively. The solid circles and open squares once again represent the in-focus condition acquired on successive days. The probe-intensity distributions in Figs. 3(b) and 3(c) also show open circles which are measurements made in the underfocus condition. The open triangles are measurements made in the overfocus condition. This is the uncertainty in the probe shape for a range of focus possible during any given experiment. The range of out-of-focus conditions assumed here represents an upper bound on the uncertainty of defocus during the SEMPA experiments. In Fig. 3(b) no significant change in the probe-intensity distribution occurs during defocus, indicating that this operating condition is diffraction limited. The Gaussian fit, given by the solid line in Fig. 3(b), has a FWHM of 0.120 μm. In Fig. 3(c), however, the underfocus condition significantly broadens the probe-intensity distribution. The Gaussian fit to the in-focus profile has a FWHM of 0.165 μm, and the Gaussian fit to the out-of-focus profile has a FWHM of 0.210 μm.

B. Data acquisition and processing

In this section we outline the processing steps used to reduce the raw SEMPA data to the line-scan profiles of domain walls which will be compared to the results of micromagnetic calculations in Sec. IV. Inherent scan asymmetries may be present in a polarization detector which

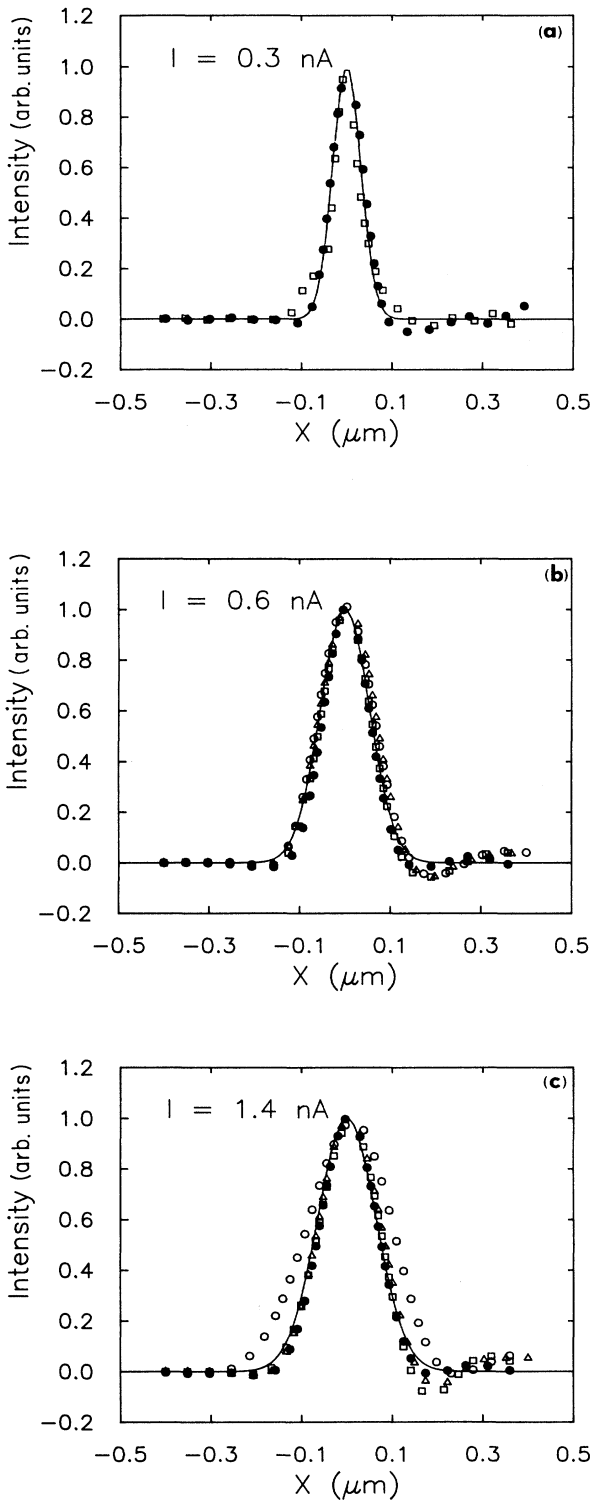

FIG. 3. Electron probe-intensity profiles for three standard SEMPA operating conditions where the incident-beam current is I=(a) 0.3 nA, (b) 0.6 nA, and (c) 1.6 nA. The solid circles and open squares are in-focus measurements on successive days. The open circles and triangles are over- and underfocus intensity distributions meant to reflect the range in the focus uncertainty during setup for a SEMPA experiment.

introduce a linear dependence of the measured magnetization on the position of the polarized electron beam in the detector.[66,67] We have drastically reduced these asymmetries,[66] and in any event at magnifications as high as 25 000× the effect would be rather small. If any residual background asymmetry remained in an image, a least-squares fit to a plane surface was done in a region of a SEMPA image where the domains are uniform. The fitted planes were subtracted from the original data.

The absolute zero of the polarization detector may change if the position of the polarized electron beam incident on the polarization detector changes from one set of measurements to another. The zero of the SEMPA images is determined by requiring that the values of the magnetization on opposite sides of a 180° domain wall be equal and opposite. If necessary, a zero-offset correction is subtracted from the data. Once the M_x and M_y data were properly calibrated, the data are added together in quadrature as $|M|=(M_x^2+M_y^2)^{1/2}$ to form the magnitude of the in-plane magnetization. The magnitude of this magnetization in the absence of any out-of-plane components should be constant across the image. We use this as a test of the accuracy of our background subtractions. Once the magnitude of the image has been determined, we form a histogram of the magnetization values within an image to determine the uncertainty with which we can determine the saturation magnetization M_s, which is constant within the film.

The domain walls were initially aligned within the SEMPA apparatus such that the wall is oriented along one of the axes of the polarization detector. Often, there are residual misalignments of the domain wall with respect to the detector axes of up to 10°. When this is the case, the images are rotated by the image-processing system to align the domain walls with the detector axes.

A region of interest within an individual image was then selected. Typically, this region was about 100×70 pixels in size. Within this region the line scans across the domain wall were summed over the 70 (nearly) identical lines in order to increase the signal-to-noise ratio. This sum was normalized to the saturation magnetization M_s (actually $M_s=|P|_{\max}$) taken from the region of a uniform domain adjacent to the domain wall. The result was the final magnetization profile across a 180° domain wall, which was compared directly to the micromagnetic calculation results in Sec. IV. The error bars present on these experimental data line scans represent the standard deviation about the mean for the individual line scans, which were averaged together.

We searched for systematic errors in the data. If there were correlations in the measurement errors between scans, the standard deviation of the average of all measurements in the set of line scans would depend upon the strength of the correlation. We investigated correlations extensively in one characteristic set of data. We computed the autocorrelation of the data up to lag 17 and found no significant correlation. A histogram of the autocorrelation in the data, at lag 1, was sharply peaked at zero and Gaussian in shape with a FWHM of 0.25. To determine if the variation in the computed values of the autocorrelation function at lag 1 was due to random sampling

effects, we simulated independent Gaussians in sets. Each set had the same number of members, which was the number of individual measurements within a single line scan. For each set the autocorrelation function at lag 1 was computed. The histograms of the autocorrelation functions at lag 1, for both the data and sets of simulated data, were similar. Quantile-quantile[73] plots of the histograms were nearly linear. We conclude that there was no evidence that individual measurements within a line scan were correlated. We estimated the standard deviation of the average magnetization along a line scan using the usual formula which applies to uncorrelated data.

III. MICROMAGNETIC WALL CALCULATIONS

A. Solution of micromagnetic equations

We calculate the micromagnetic structure present in surface domain walls by following methods used by Brown and LaBonte,[10] LaBonte,[11] Aharoni,[12–17] and Schabes *et al.*[25,26] The equilibrium magnetization configuration of domain walls in ferromagnetic materials can be thought to result from the minimization of the total system energy. The energy of a ferromagnetic system is composed of (1) the mean-field exchange energy E_{ex} between nearest neighbors, characterized by the exchange-coupling constant A (erg/cm); (2) the magnetocrystalline anisotropy energy E_K, which describes the interaction of the magnetic moments with the crystal field characterized by the constant K_v (erg/cm^3); (3) the surface magnetocrystalline anisotropy energy E_{Ks}, which corrects for broken symmetry near surfaces in the interaction of the magnetic moments with the crystal field and is characterized by the constant K_s (erg/cm^2); (4) the magnetostatic self-energy E_s, which arises from the interaction of the magnetic moments with the magnetic fields created by discontinuous magnetization distributions both in the bulk and at the surface; (5) the external magnetostatic field energy E_h, which arises from the interaction of the magnetic moments with any externally applied magnetic fields; and (6) the magnetorestrictive energy E_r, which arises when mechanical stress (strains) are applied to a ferromagnetic material, thereby introducing effective anisotropy into the system characterized by K_m (erg/cm^3). We do not consider effects due to thermal fluctuations here.

We solve for the magnetization distribution in a domain wall by considering a constrained boundary-value problem in two spatial dimensions with the constraint of constant magnetization M_s. We approximate the continuous magnetization distribution of a ferromagnet by a discrete magnetization distribution, as shown in Fig. 4. The ferromagnet is seen in cross section. The magnetization is discretized in the x-z plane of the cross section, but is uniform in y. Each individual discretized magnetization cell, interior to the array, will be addressed by the $(\mathbf{x},\mathbf{z})$ coordinate of its centroid as $(J\Delta, I\Delta)$, where Δ is the square discretization cell width, and J and I are integers. There are N_x cells along x and N_z cells along z interior to the wall region. There is one column of boundary cells at either side of the discretized region. These boundary cells (conditions) reflect the continuous uniform magnetization distribution present within the domains themselves on either side of the wall which impose Dirichlet boundary conditions. The Dirichlet boundary conditions, which are shaded in Fig. 4, are positioned at the far left and far right edges of the discretized wall region at $J=1$ and N_x+2. The boundary conditions at the top and bottom surfaces of the film, $I=1$ and N_z+2, are of the Neumann type. In the absence of surface anisotropy, the normal derivative of the magnetization distribution at the surface is zero.[11,74] In the presence of surface anisotropy, we use the Rado-Weertman boundary conditions.[74,75] The surface boundary elements at $I=1$ and N_z+2 are linear elements and are used specifically to incorporate surface anisotropy effects. The surface cells, which are indicated by solid squares in Fig. 4, are differentiated from the volume cells which are shown as solid circles.

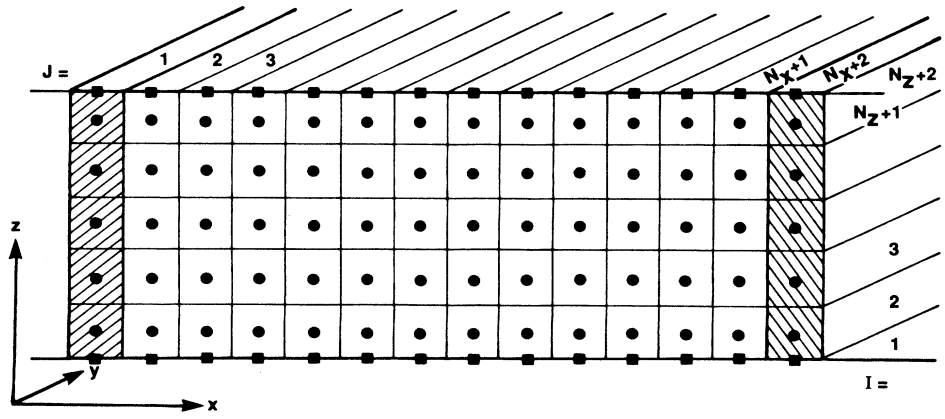

FIG. 4. Discretization array for the calculation of micromagnetic structure. The array has $N_x \times N_z$ interior cells. The Diriclet boundary conditions are imposed at the left and right shaded columns, and Neumann boundary conditions are applied to the top and bottom surface cells. Each interior cell is square of edge length Δ. The surface cells are one dimensional and of length Δ.

Fundamental to our solution of the micromagnetic equations is the assumption that the bulk saturation magnetization M_s (emu/cm^3) is constant microscopically throughout the ferromagnet. Throughout this paper we will use the parameter M_s to represent saturation magnetization at room temperature. For the systems being considered here, there is little deviation in M_s from the 0-K value, although we use the room-temperature values. We represent the value of the magnetization vector $\mathbf{M}(\mathbf{r})$ at each point within the ferromagnet as the saturation magnetization multiplied by the direction cosines, that is,

$$\mathbf{M}(\mathbf{r})=(M_x(\mathbf{r}), M_y(\mathbf{r}), M_z(\mathbf{r}))=M_s\boldsymbol{\alpha}(\mathbf{r})=M_s(\alpha(\mathbf{r}), \beta(\mathbf{r}), \gamma(\mathbf{r})) .$$

The constraint equation implied by the constant magnetization assumption is $|\boldsymbol{\alpha}(\mathbf{r})|=1$.

The individual contributions to the wall energies in this continuum model are calculated by integrating the energy expressions over the cross section of the wall in the **x-z** plane. The energies are expressed in energy/unit-length. The energy integrals below are integrated over the cross sectional area of the wall ($d\sigma$). The exchange energy E_{ex} in the continuum approximation is given by

$$E_{\text{ex}}=\int A(|\nabla\alpha|^2+|\nabla\beta|^2+|\nabla\gamma|^2)d\sigma . \quad (1)$$

The exchange parameter A can be extracted from spin-wave theory,[29,76,77] which shows that $A=A'M_s^2=DS/2V$, where D is the spin-wave dispersion parameter, S is the spin per atom, V is the volume per atom, and $d\sigma$ is the incremental cross-sectional area. The spin-wave dispersion parameter D is related to the exchange constant J in the Heisenberg Hamiltonian by $D=2JSa^2$, where a is the lattice spacing. This relationship is true for spin-wave modes along bcc [100], bcc [110], fcc [110], and fcc [100] directions.

The volume magnetocrystalline anisotropies for uniaxial (easy axis in **y**) E_{Ku}, and cubic crystals E_{Kc}, are given by the following expressions, respectively:[16,18]

$$E_{Ku}=\int [K_{u1}(1-\beta^2)+K_{u2}(1-\beta^2)^2]d\sigma , \quad (2)$$

$$E_{Kc}=\int [K_{c1}(\alpha^2\beta^2+\beta^2\gamma^2+\gamma^2\alpha^2)+K_{c2}\alpha^2\beta^2\gamma^2]d\sigma , \quad (3)$$

where the bulk anisotropy constants for cubic K_c and uniaxial K_u symmetry can be determined from torque magnetometry measurements. The energy due to magnetostriction can be included in the expression for the uniaxial anisotropy by appropriately adjusting the value of the anisotropy constant.[78] The surface magnetocrystalline anisotropy energy E_{Ks} is given by

$$E_{Ks}=\tfrac{1}{2}\int [K_{s1}\gamma^2+K_{s2}\alpha\beta]ds , \quad (4)$$

where the integration is along the (linear increment ds) boundary at the film surfaces. The symmetry of the surface anisotropy energy was determined by Rado and coworkers.[79,80]

The self-magnetostatic field energy E_s can be represented in a number of equivalent forms, but for our purposes the most convenient representation is

$$E_s=-\tfrac{1}{2}\int \mathbf{H}_s\cdot M_s\boldsymbol{\alpha}\, d\sigma , \quad (5)$$

where the self-field $\mathbf{H}_s$ is determined from the scalar magnetic potential as $\mathbf{H}_s=-\nabla\Phi$. The magnetic scaler potential Φ satisfies $\nabla^2\Phi=4\pi M_s\nabla\cdot\boldsymbol{\alpha}$ inside the ferromagnet, $\nabla^2\Phi'=0$ outside the ferromagnet, and at the surface $\Phi=\Phi'$ and $-d\Phi/dz+4\pi M_s\gamma=-d\Phi'/dz$. The regularity of Φ' at infinity is also required. This can be guaranteed by solving for the potential using Green's-function methods. The calculation of this self-field energy is the most computationally intensive aspect of solving the micromagnetic equations. The external field energy E_h for an applied field of $\mathbf{H}_0$ is simply given as

$$E_h=-\int \mathbf{H}_0\cdot M_s\boldsymbol{\alpha}\, d\sigma . \quad (6)$$

In order to calculate domain-wall microstructure in ferromagnets, the time evolution of a magnetization configuration inside a ferromagnet, which is described by the Landau-Lifshitz-Gilbert equation, must be solved. The Landau-Lifshitz-Gilbert equation has been examined experimentally and theoretically[28,29,32,81,82] and found to yield an accurate description of the time evolution of a magnetic moment of fixed magnitude in a magnetic field. This equation has the following form.

$$\frac{d\mathbf{M}}{dt}=\omega'\mathbf{M}\times\mathbf{H}_{\text{eff}}+\frac{\lambda'}{M_s}\mathbf{M}\times\mathbf{M}\times\mathbf{H}_{\text{eff}} . \quad (7)$$

The parameters are given by $\omega'=\omega/(1+\lambda^2)$ and $\lambda'=\omega\lambda/(1+\lambda^2)$. Here the gyromagnetic ratio $\omega=\omega_e g/2$ is determined from the free-electron value of ω_e and the spectroscopic splitting factor, $g=2$. The gyromagnetic ratio ω, the damping parameter λ, and the magnitude of the effective fields determine the times scales of interest. For our time-domain simulations, we use the free-electron gyromagnetic value of $\omega=1.78\times10^7$ (Oe sec^{-1}). The damping parameter λ is not well known. We have used values of λ between 0.005 and 2.0, and found that for the calculation of equilibrium magnetization configurations in domain walls in uniform ferromagnetic systems, it is not important.[83] The effective magnetic field on each magnetic moment is determined from the total system energy E_{tot} as

$$\mathbf{H}_{\text{eff}}=-\frac{\partial E_{\text{tot}}}{\partial(M_s\boldsymbol{\alpha})} . \quad (8)$$

The effective magnetic field incorporates all the effects of exchange, anisotropy, external fields, and demagnetizing fields. For the analysis of the equilibrium micromagnetic structure of simple two-dimensional domain walls presented in this paper, we do not integrate Eq. (7) direct-

ly. Instead, we note that for an equilibrium magnetization distribution, $d\mathbf{M}/dt=0$, which implies that the effective field $\mathbf{H}_{\text{eff}}$ must be parallel to the magnetization $\mathbf{M}$. We relax the magnetization configuration iteratively by positioning each magnetization vector along the effective-field vector direction throughout the mesh of Fig. 4. The initial condition from which we begin the iteration procedure is one where the y component of the magnetization, $M_y(z)$, is linearly interpolated across the domain wall. The other two magnetization components are equal and of size $0.5[1-M_y^2(z)]^{1/2}$.

When the largest residual of a single value of $(\mathbf{M}\times\mathbf{H}_{\text{eff}})/|\mathbf{M}|\,|\mathbf{H}_{\text{eff}}|$ decreases below a convergence minimum, we stop the iteration process. We took as our convergence minimum for terminating the calculation the value of the largest relative change in the largest component of the direction cosines, typically a value of 0.002. This implies that the largest relative change in angle was less than 0.25° for the single largest change of any discretized magnetization in the wall. We have found that equilibrium domain-wall configurations determined from this energy minimization scheme agree extremely well with configurations determined by solving the Landau-Lifshitz-Gilbert equation directly.[83] As we are only interested in equilibrium configurations for uniform systems here, we use the more economical energy minimization scheme to determine equilibrium domain-wall configurations. We note that for more complex systems or in the presence of grain boundaries which may serve as nucleation sites, the solution of the Landau-Lifshitz-Gilbert equation is necessary for accurate results.[28,29] For completeness we include in Appendix A explicit expressions for the energies and effective-field components used in our micromagnetics calculations for the discretized grid shown in Fig. 4.

B. Micromagnetic structure of domain walls

We performed simulations for the specific examples which we examined using SEMPA. We present micromagnetic domain-wall structure for a single-crystal (whisker) of Fe(100) and for several thin films of Permalloy ($Ni_{0.81}Fe_{0.19}$). Bulk parameters were used for all calculations. The exchange-coupling constants A were 2.1×10^{-6} erg/cm for Fe (Refs. 29 and 77) and 1.05×10^{-6} erg/cm for Permalloy.[29,77,84] The saturation magnetization values M_s were 1714 emu/cm^3 for Fe (Ref. 78), and 813 emu/cm^3 was measured for Permalloy. A cubic induced anisotropy constant K_c $(=K_{c1})$ of 4.7×10^5 erg/cm^3 was used for Fe.[78] No magnetostriction or surface anisotropy terms were included in the Fe calculations. A test calculation showed that the magnetostriction made a negligible contribution to the total system energy. The contribution of the surface anisotropy was also small and will be discussed in Sec. IV C 2. The uniaxial induced anisotropy constant K_u $(=K_{u1})$ for Permalloy, incorporating both the intrinsic anisotropy (913 erg/cm^3) and magnetostriction (840 erg/cm^3), was measured. The total uniaxial anisotropy parameter used for the Permalloy samples was 1743 erg/cm^3. No surface anisotropy terms were included in the calculations of the Permalloy micromagnetic structure. In addition to these bulk magnetic parameters, our micromagnetics calculation took as input the boundary conditions at $J=1$ and N_x+2, the film thickness (or periodic boundary conditions), the cell density, and a convergence criteria indicating when to stop the minimization scheme.

1. *Infinite crystals and thick films*

In Fig. 5 the magnetization distribution for a cross section near the surface of a 180° domain wall in Fe is calculated. The arrows indicate the direction and magnitude of the magnetization vector in the x-z plane of the wall cross section. The boundary conditions used have the magnetization going out of the page $(-M_y)$ on the left and into the page $(+M_y)$ on the right. A bulk Bloch wall runs vertically through the center of the structure. In a Bloch wall the magnetization rotates in the plane of the wall. The bulk Bloch wall terminates in a surface Néel wall, where the magnetization rotates perpendicular to the wall. Both structures are visible in the figure. In this calculation the total film thickness was 0.5 μm.

As a first test of our micromagnetics calculations, we compare our energy-minimization calculation with a variational calculation of 180° Bloch wall in an infinitely thick uniaxial crystal. In the variational formulation the functional form for the magnetization is determined by minimizing the energy of the system. This problem can be solved in closed form using variational principles[85] because there is no contribution from the magnetostatic self-energy. We note that magnetization configurations which produce minimum-energy one-dimensional walls have equal exchange and anisotropy energies. In Fig. 6(a) we show the spatial distribution of the magnetization

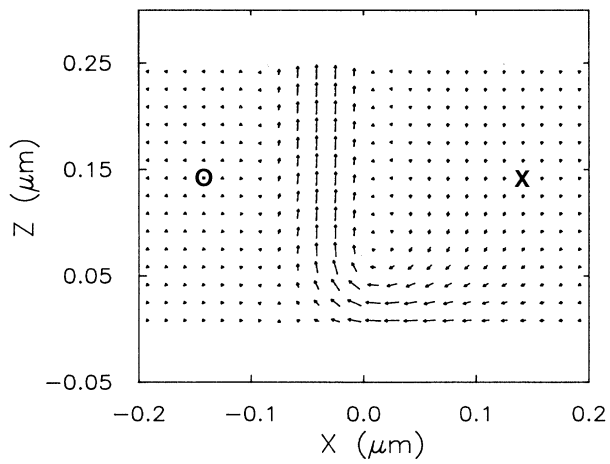

FIG. 5. Cross section through a calculated 180° wall in a 0.5-μm-thick Fe (100). The magnetization direction and magnitude in the plane of the cross section are indicated by the direction and length of the magnetization vectors. The bulk Bloch wall and surface Néel wall are seen in the bulk and at the surface, respectively. The penetration depth of the wall from the surface is on the order of a Bloch-wall width.

across a bulk Bloch wall for a fictitious "uniaxial Fe crystal." The micromagnetic parameters used were identical to those specific above for Fe, but the symmetry of the magnetocrystalline anisotropy was selected to be uniaxial. Periodic boundary conditions were used (in **z**). The periodic boundary conditions equate the top layer of the discretized magnetization with that in the bottom layer for a two-dimensional grid. In this way we extracted the one-dimensional wall solution from a two-dimensional grid, without enforcing *a priori* the structure of the wall. The region of the film cross section that was discretized was 0.7 μm wide and $\Delta=0.007$ μm. The solid points are results from our micromagnetic calculation, whereas the solid line is the variational result. The contributions to the wall energy due to anisotropy and exchange, as determined by the variational method, are equal, and for this example each is equal to $2(AK)^{1/2}=1.987$ erg/cm^2. Our calculation determines the exchange energy to be 1.993 erg/cm^2 and the anisotropy energy to be 1.963 erg/cm^2.

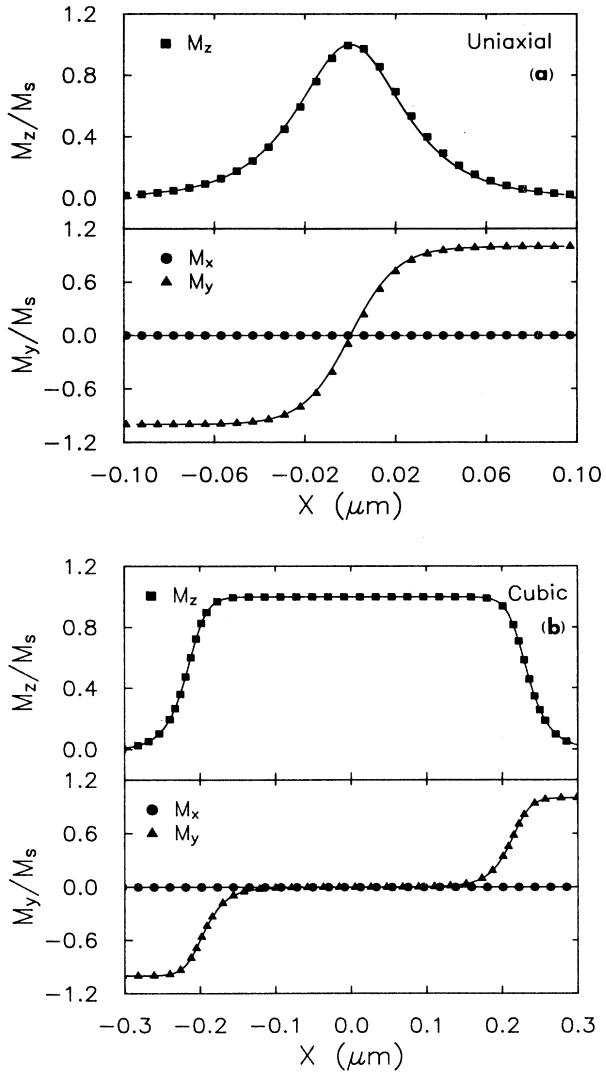

FIG. 6. (a) Magnetization profiles of a 180° Bloch wall in an infinite Fe crystal with a fictitious uniaxial anisotropy. The solid points are the results of our micromagnetic calculation, and the solid line is the variational method result. (b) Magnetization profiles for a 180° Bloch wall in an infinite Fe crystal with cubic anisotropy, but no magnetostriction. The walls breaks into two 90° walls without the presence of a surface or magnetostriction.

If the anisotropy is allowed to assume cubic symmetry, as it does in real Fe, classical micromagnetic theory[85] indicates that the bulk Bloch wall should separate into two 90° walls separated by infinity. This is the result for zero magnetostriction. We tested our micromagnetics calculation on this system, realizing, of course, that we could not discretize an infinite grid. The spatial dependence of the magnetization in a 180° domain wall for bulk Fe with cubic anisotropy and no magnetostriction is shown in Fig. 6(b). Although the width of the discretized wall cross section was only 0.7 μm, we see that the bulk wall broke into two separate 90° walls separated by as large a distance as possible within the rigid boundary conditions. The total energy for a (100)-oriented wall in cubic anisotropy material determined by variational methods should be $2(AK)^{1/2}=1.987$ erg/cm^2.[85] We determine the total wall energy to be 1.983 erg/cm^2, 0.988 erg/cm^2 for anisotropy and 0.995 erg/cm^2 for exchange. Note that the wall energy of the cubic symmetry material which separates into two 90° walls is half of that of the uniaxial material.

To illustrate the effect that finite film thickness has on determination of the bulk-domain-wall magnetization distribution in Fe, we calculated the magnetization distribution in a 0.5-μm-thick Fe single crystal for both cubic anisotropy and a fictitious uniaxial anisotropy. The domain wall in a uniaxial infinite crystal forms a single 180° wall. This case is important because, unlike in the cubic case, we can make direct comparisons between the infinite-thickness variational result and the micromagnetics results for finite-thickness films.

In Figs. 7(a) and 7(b) we show magnetization distribution across 180° bulk domain walls in Fe for the uniaxial and cubic cases, respectively. The wall magnetization profiles are taken from the center ($z=0.25$ μm) of the film and are characteristic of the bulk. The solid points in Fig. 7(a) are calculated results from the full micromagnetic calculation, and the solid line is once again the variational method result for the infinite crystal for comparison. The discretized region was 0.7 μm wide and 0.5 μm thick. Each square cell was 0.0166 μm on a side. The magnetization distribution was not sensitive to the mesh density, as doubling the number of cells in both the x and z direction did not change these results. Widening the discretization region by up to a factor of 2 did not significantly alter these results. Furthermore, increasing the thickness of the film to 0.7 μm did not change the magnetization distribution either at the surfaces or interior to the film. Large increases in the thickness of the film did produce magnetization configurations which were no longer symmetric about the midplane of the film. These configurations may differ little in energy, and thus the true global minimum is difficult to identify. The surface-domain-wall distributions are relatively insensitive to the

non-symmetric configuration in bulk. The deviation of the finite-thickness film magnetization profiles from those for the infinite crystal result from magnetic-flux coupling between the two opposite film faces. This adds a negative component of the wall magnetization M_z on either side of the wall. This behavior can also be identified in the cross-sectional view of the domain wall of Fig. 5, where some return flux can be seen on the far right of the figure. This return flux couples the two sides of the film away from the Bloch wall and is identified by the small downward-directed arrows at the right in Fig. 5. We note that the finite-thickness bulk domain wall has flux returning (M_z) on either side of the wall, as originally predicted by Brown and LaBonte,[10] and hence we term this configuration a Brown wall. The Brown wall is different in structure than the infinite crystal wall, the Landau-Lifshitz wall[2] of Fig. 6(a), which has no return flux (M_z). This phenomenon is related to the presence of the surface and occurs for a wide range of magnetic parameters, including materials as soft as ferromagnetic glasses.[54] There is no experimental method to measure Bloch walls interior to films with the necessary spatial resolution in order to determine which configuration is realized.

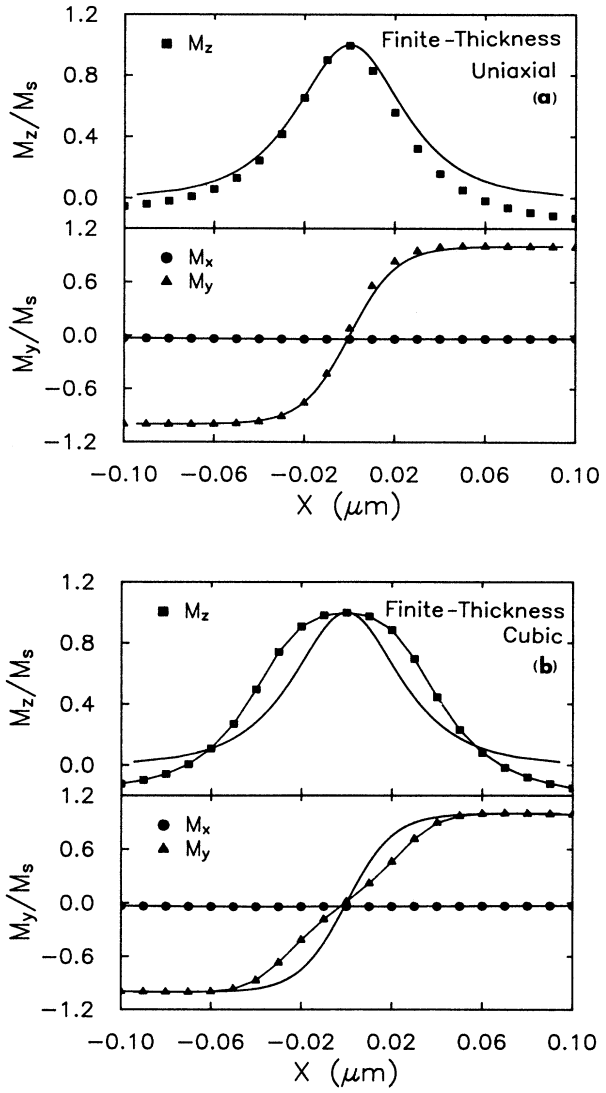

FIG. 7. (a) Magnetization profiles of a 180° Bloch wall taken from the center of a 0.5-μm-thick Fe crystal with a fictitious uniaxial anisotropy. The solid points are the results of our micromagnetic calculation, and the solid line is the variational method result for an infinite crystal. (b) Magnetization profiles taken from the center of a 180° Bloch wall in a 0.5-μm-thick Fe crystal with cubic anisotropy, but no magnetostriction. The wall does not break into two 90° walls in the presence of a surface without magnetostriction present. The solid line (no points) is the variational result for uniaxial anisotropy for an infinite crystal. This illustrates the subtle magnetization profile changes in the Bloch wall between uniaxial and cubic symmetry crystals.

In Fig. 7(b) the magnetization profile from a 180° Bloch wall in a finite-thickness film which has cubic anisotropy shows that the bulk Bloch wall does not separate into two 90° walls as it did for the infinite-thickness-film case. The solid points are the results for the micromagnetic simulation with a solid line drawn through the solid points to guide the eye. The other solid line is the variational result for the uniaxial Fe crystal. No magnetostriction was included in our calculation, yet the wall did not break into two 90° walls. The magnetostatic energy of the surface (e.g., in the x-y plane at $z=0$ in Fig. 5) is large enough to bind the wall together.

The 180° Bloch-wall magnetization profiles in bulk are nearly symmetric (when compared to those profiles observed on the surface, as we will show), as shown in Figs. 7(a) and 7(b). Furthermore, we observe that the bulk Bloch wall in a cubic material is wider than the corresponding wall in a uniaxial material with the same magnetic parameters. The flux feeding back along the side of the wall is seen in the negative values of the calculated M_z magnetization distribution.

Using SEMPA, we are only able to measure the surface magnetization distribution, not the bulk. Any connection that we can make to the bulk structure of the domain wall must be made through the surface magnetization distribution. In Fig. 8 we illustrate some of the general features of our domain-wall calculation that we will be comparing to our SEMPA measurements. This figure displays the surface and bulk magnetization profiles for an Fe(100) crystal with cubic anisotropy, but without magnetostriction, as shown in cross section in Fig. 5. Figure 8(a) shows the surface magnetization profile extracted from the bottom layer of cells, at $z=0.0$, in the discretized array, and for comparison Fig. 8(b) shows the bulk magnetization profile extracted from the center layer of cells, at $z=0.25$, in the array. The asymmetry in the surface-domain-wall profile is evident. The surface wall is also much wider than the corresponding wall in bulk. Further, we note that the peak in the M_x magnetization distribution of the Néel wall on the surface is offset from the peak in the bulk M_z magnetization distribution of the bulk Bloch wall. This offset is Δ_{wall} and is an important feature which can be measured with SEMPA as described in Sec. IV.

In order to test the sensitivity of the micromagnetics results to the values of the input parameters, we systematically varied the micromagnetic parameters by ±5% of their nominal values. That is, we let $A = 2.10 \pm 0.105 \times 10^{-6}$ erg/cm, $M_s = 1714 \pm 86$ emu/cm^2, and $K_c = 470\,000 \pm 23\,500$ erg/cm^3, and then compute the domain-wall structures. These variations reflect the experimental uncertainty in determining these parameter values. In each case the discretized region was 0.7 μm wide and 0.5 μm thick and $\Delta = 0.0166$ μm. The convergence criteria, the largest allowed change in a single component of the magnetization at a single cell in the array prior to exiting the program, was 0.002. In Fig. 9(a) the nominal surface-domain-wall magnetization distribution is given by the solid points. The error bars which result from deviations due to variations of the magnetic parameters and are the maximum total variation of the domain-wall profile from the nominal profile. Furthermore, the error bars were made symmetric by reflecting the largest variation about the nominal value. The asymmetry in the error bars across the profile reflects the sensitivity of the surface domain wall to the material's stiffness. As the exchange parameter A is decreased (or the anisotropy parameter K increased), for example, the wall can turn into plane faster (more sharply) at the surface, thereby affecting the rising edge of the profile more dramatically. The largest deviations are less than ±5.0%. The average deviation over the whole

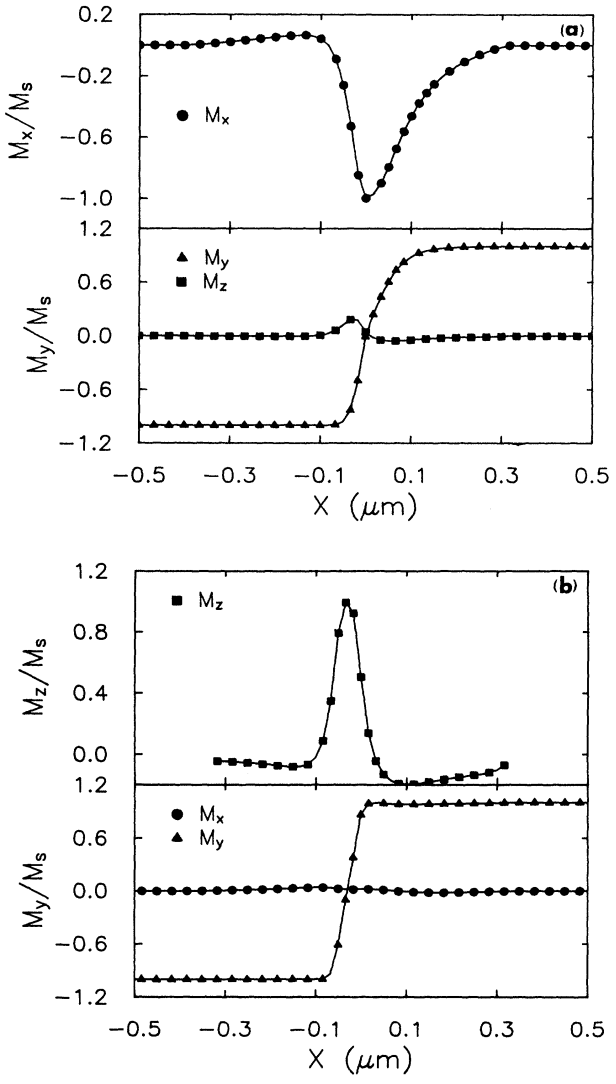

FIG. 8. (a) Surface magnetization profiles $z=0$ of a 180° Bloch in a 0.5-μm-thick Fe crystal with cubic anisotropy. (b) Corresponding bulk magnetization distribution taken from the center of the film. The surface wall is asymmetric, while the bulk wall is largely symmetric. The surface wall peak is shifted from the bulk wall peak by Δ_{wall}.

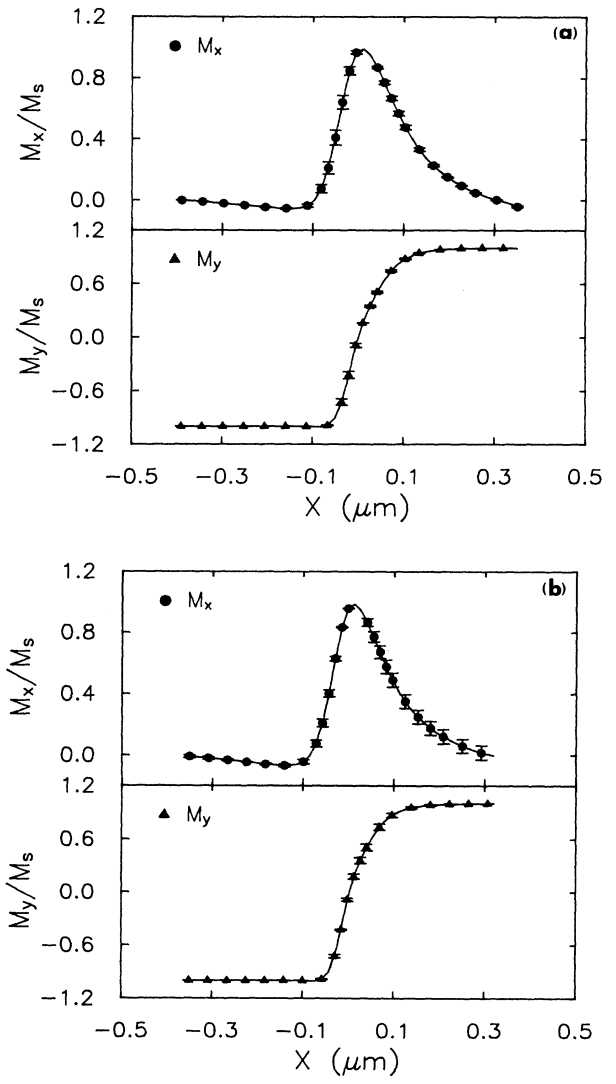

FIG. 9. (a) Effect of varying the magnetic parameter values input into the micromagnetics calculation by ±5.0%. (b) Effect of varying the grid density and mesh size input into the micromagnetics calculation. The error bars indicate the total deviation of the results.

profile is under ±2.0%.

The sensitivity of the calculated domain-wall magnetization profiles to the variation in the grid size and density was also investigated. The film thickness was varied from 0.4 to 0.7 μm, and the discretized width was varied from 0.5 to 0.8 μm. The cell size was varied between $\Delta=0.0166$ and 0.008 33 μm. The results of these simulations are shown in Fig. 9(b). Once again, the nominal surface-domain-wall magnetization distribution (0.5 μm thick, 0.7 μm wide, and $\Delta=0.0166$ μm) is given by the solid points. The error bars are the maximum deviations due to variations of the geometric parameters, symmetrically reflected about the nominal value. The largest deviations are ±5.0%, but the average of the deviations is nearly ±2.0%. The largest deviations occur as a result of selecting a small discretization-region width which clamps the tail of the wall-magnetization profile when the boundaries are too close together. This is the cause of the larger error bars on the tail (right-hand side) of the wall. By selecting a large enough discretization region, deviations due to the presence of the boundaries can be minimized. We found that for some meshes the minimization procedure produced metastable equilibria where the energy of the configuration was clearly higher than the minimum. Interestingly, these metastable equilibria can be obtained by integrating the Landau-Lifshitz-Gilbert equations in time or by minimizing the magnetic energy of the system. The metastable equilibria produce surface domain profiles which are different than the minimum-energy configuration. In order to investigate the possibility of realizing any of these metastable states experimentally, it would be necessary to include the effects of thermal fluctuations. This is outside of the scope of the present work. In any case these metastable equilibria have been excluded from Fig. 9(b).

2. *Magnetically thin films*

The structure of domain walls in thin films is very different from that of thick (or infinite-thickness) films.[3,4,10–22] The term "asymmetric Bloch wall" was coined by LaBonte[11] to describe the vortex domain-wall structures which occur in films which are too thin to support bulk Bloch walls and yet too thick to support Néel walls. The calculated cross section of an asymmetric Bloch wall in a 0.160-μm-thick Permalloy film is shown in Fig. 10(a). The magnetization is out of the page ($-\mathbf{y}$) to the left of the wall and into the page ($+\mathbf{y}$) to the right of the wall. We find that when the two surfaces are close together, they couple magnetostatically, and a vortex structure results. There is no well-defined Bloch wall in the interior of the film, although the strong magnetization directed along $+\mathbf{z}$ eventually degenerates into a Bloch wall as the thickness of the film is increased. The width of the surface Néel wall is a function of the film thickness for asymmetric Bloch wall (vortex) structures.

The magnetization from the top layer of cells in the mesh is shown in Fig. 10(b). This is a 180° surface domain wall in a 0.160-μm-thick Permalloy film. The magnetic parameters used in this calculation are those specified above for Permalloy. The discretization region was 0.800 μm wide and 0.160 μm thick. The cell size was $\Delta=0.0160$ μm, and the convergence criteria was 0.005. The asymmetric shape of the surface-domain-wall profile is as evident for the asymmetric Bloch wall as it was for the thick films which supports bulk Bloch walls. Surface Néel walls seem to be asymmetric in general.

We tested the sensitivity of the surface magnetization distributions in 180° walls in thin Permalloy films to variations in the input parameters prior to comparison with experimental SEMPA measurements. We again systematically varied the micromagnetic parameters and the film thickness by ±5% of their nominal values to include the experimental uncertainty in their determination. That is, we let $A=1.05\pm0.051\times10^{-6}$ erg/cm, $M_s=813\pm40$ emu/cm^2, and $K_u=1743\pm87$ erg/cm^3, and then we compute the domain-wall structure. In each case the discretized region was 0.800 μm wide and 0.160 μm

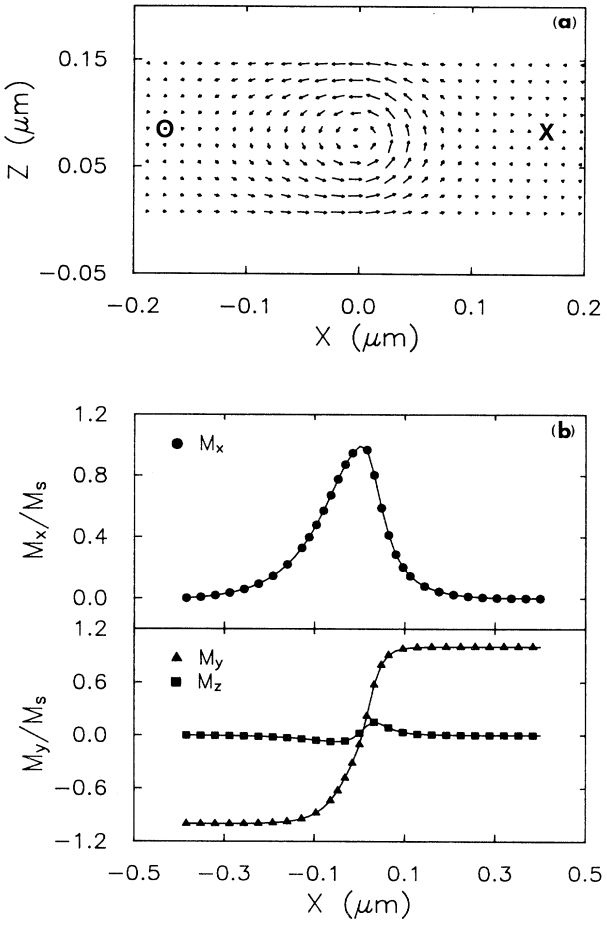

FIG. 10. (a) Cross section through a 180° wall in a 0.16-μm-thick Permalloy film. The magnetization direction and magnitude in the plane of the cross section is indicated by the direction and length of the magnetization vectors. The bulk Bloch wall and surface Néel wall are seen in the bulk and at the surface, respectively, in Fe are replaced with a vortexlike structure called an asymmetric Bloch wall. (b) Surface magnetization profile for the wall shown in (a).

thick, and $\Delta=0.016$ μm. The film thickness was $t=0.160\pm0.005$ μm. The convergence criterion was 0.005. In Fig. 11(a) the nominal surface-domain-wall magnetization distribution is given by the solid points. The error bars are once again the total deviations due to variations of the magnetic parameters. The largest deviations are less than $\pm4.0\%$, with the average deviations over the whole profile under $\pm2.0\%$. The sensitivity of the calculation to grid size and density was also investigated. Discretization widths were varied from 0.480 to 0.800 μm. The cell size was varied between $\Delta=0.020$ and 0.08 μm. The results of these simulations are shown in Fig. 11(b). The largest deviations are $\pm5.0\%$, but the average of the deviations is nearly 2.0%. The largest deviations again occur as a result of selecting a small grid width which clamps the tail of the wall magnetization profile. By selecting a large enough grid, deviations due to the presence of the boundaries can again be minimized. Once again, we would like to emphasize that metastable equilibria can be found for some mesh densities. The results shown here exclude these higher-energy states.

The effect of varying the exiting convergence criteria is shown in Fig. 11(c) for a 0.16-μm-thick Permalloy film of cell size $\Delta=0.016$ μm and discretization region width of 0.80 μm. The curves in Fig. 11(c) illustrate the effect of exiting the minimization procedure prematurely. The convergence criteria, given by the largest change in any of the direction cosines in the grid, were 0.05, 0.01, 0.005, and 0.0001, respectively, for the curves in M_x, beginning

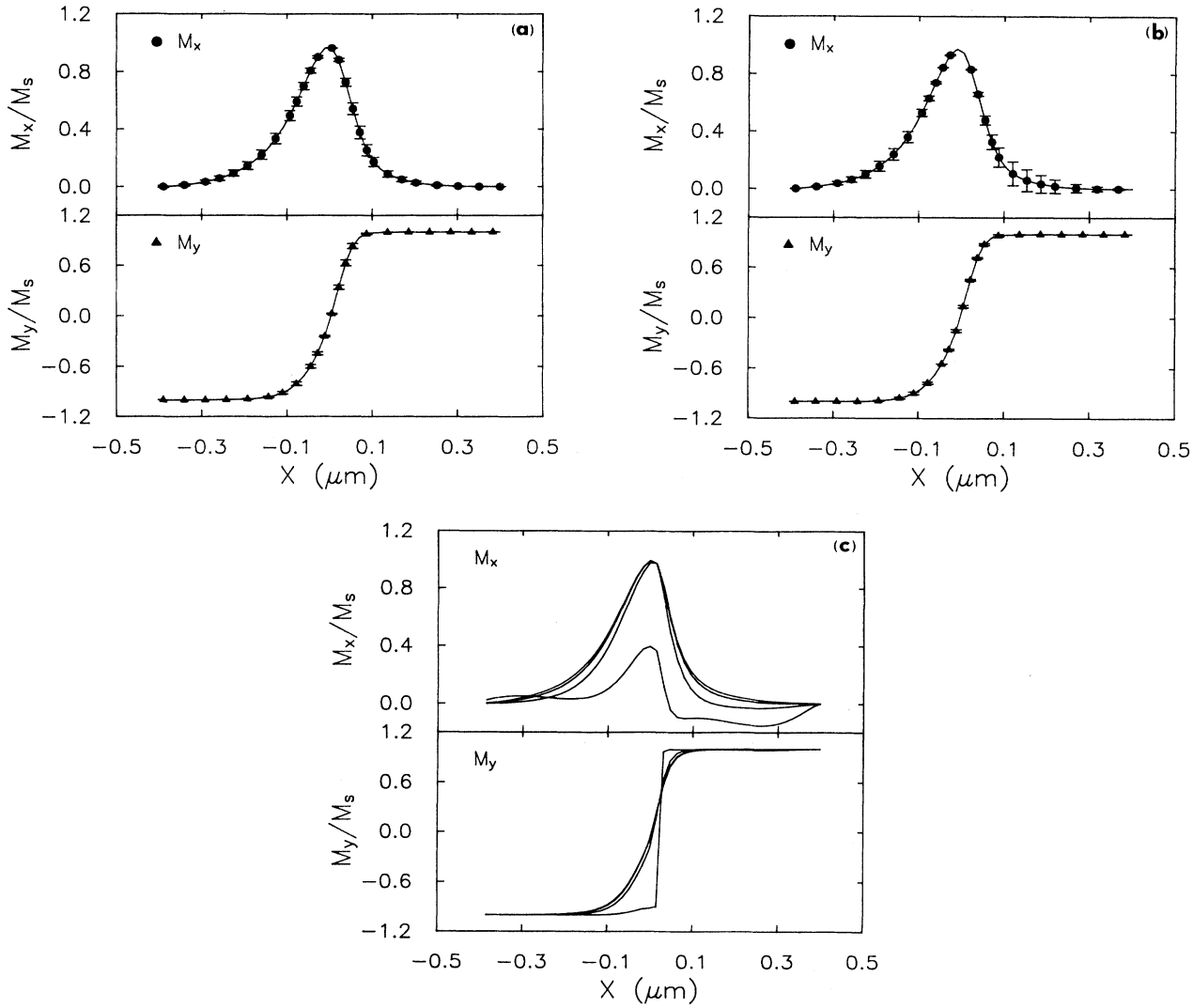

FIG. 11. (a) Effect of varying the magnetic parameter values input into the micromagnetics calculation by $\pm5.0\%$ and the thickness of the film by ±0.005 μm for the 0.16-μ-thick Permalloy film. The error bars indicate the total deviation of the results. (b) Effect of varying the grid density and mesh size input into the micromagnetics calculation. The error bars indicate the total deviation of the results. (c) Effect of varying the exiting convergence criteria in the micromagnetic simulation. The exiting criteria are 0.05, 0.01, 0.005, and 0.0001 beginning with the lowest curve and moving up for M_x, and beginning with the upper curve and moving down for M_y.

with the lowest curve and moving upward. The curves in M_y start with the discontinuous curve for a convergence criterion of 0.05 and move downward. Minimal changes occur in the surface-domain-wall magnetization distribution for convergence criteria less than 0.005. We use this value in most of our simulations. It should be noted that the energy-minimization scheme does not ensure that a global minimum is reached, only a local minimum.

IV. COMPARISON BETWEEN SEMPA MEASUREMENTS AND MICROMAGNETIC CALCULATIONS OF 180° WALLS

A. 180° surface domain walls in Fe(100)

SEMPA domain-wall images in Fe were taken from single-crystal Fe(100) whiskers.[86] Fe was selected for study because its magnetic properties are well known and we could obtain sample crystals with excellent crystalline and chemical structure, making it an ideal test sample. The whiskers were sputtered with 2-keV argon-ion beams, with cyclic annealing to 500 °C for 2 min during sputtering. The sputtering process was continued and monitored using Auger electron spectroscopy until the oxygen peak at 535 eV was removed. The crystal was annealed at 600 °C for 3 min to remove the 20 Å or so deep sputter damage of the whisker surface. Sharp reflection high-energy electron diffraction (RHEED) spots from the whisker indicated that the surface was atomically well ordered. Once the whisker was cleaned and annealed, we imaged the magnetic microstructure using SEMPA. We note that the whisker thickness, which was about 20 μm, represents a thick film (crystal) micromagnetically, and hence the total whisker thickness variation due to

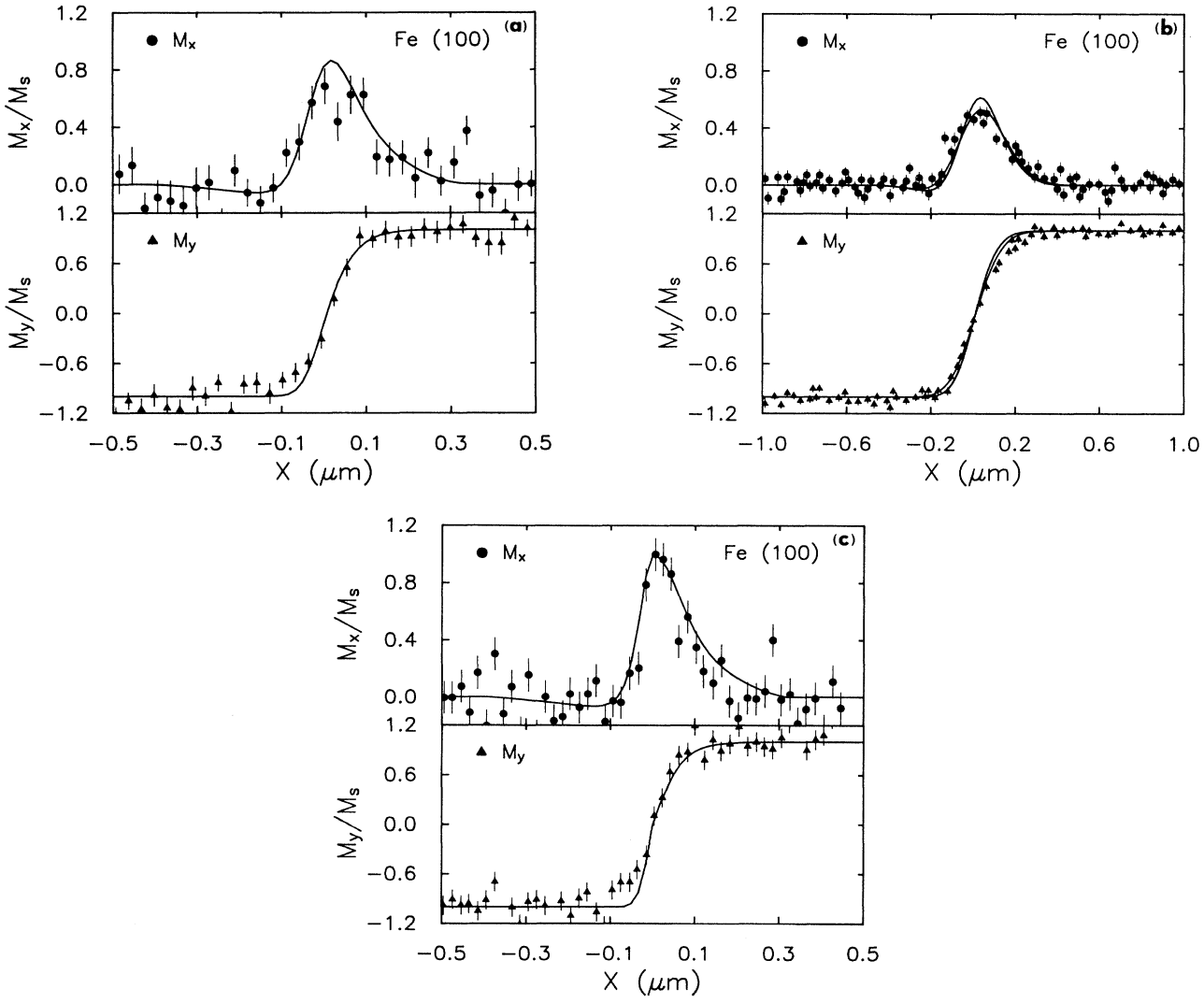

FIG. 12. Magnetization profiles for a 180° surface domain wall in Fe(100). (a) Data were acquired with $I=0.3$ nA, and the solid line is the result of micromagnetic theory convolved with the probe-intensity distribution of Fig. 3(a). (b) Data were acquired with $I=1.6$ nA, and the solid lines are the results of micromagnetic theory convolved with the limiting probe-intensity distributions of Fig. 3(c). (c) Data are from Ref. 53, and the solid line is the raw result of micromagnetic theory.

sputtering is unimportant. Additionally, we note that measured surface-domain-wall profiles were identical for annealed and unannealed[53] Fe samples. This is consistent with the length scale for sputter damage, of about 20 Å, being significantly shorter than the surface magnetic wall thickness, which is on the order of a Bloch-wall width.

In Figs. 12(a)–12(c) results of SEMPA measurements of 180° surface domain walls in Fe(100) whisker are compared with the results of micromagnetic theory. The data of Figs. 12(a) and 12(b) are extracted from SEMPA images as described in Sec. II B. In Fig. 12(a) the incident-beam current was $I=0.3$ nA, and the probe diameter was nominally 0.070 μm. The experimental data are shown by solid circles (M_x) and solid triangles (M_y). All experimental line-scan data will be presented in this way. The error bars represent the standard deviation about the mean of the line scans, which were averaged together to form this single line scan. The solid lines in Fig. 12(a) are the results of convolving the calculated surface-domain-wall magnetization distribution for a 0.5-μm-thick Fe(100), as in Fig. 8(a), with the measured 0.070-μm probe-intensity profile of Fig. 3(a). We chose not to deconvolute the experimental data as it would introduce further noise in the data. Excellent agreement is found between the model calculations and the experimental results.

To show the reproducibility of the data, the data of Fig. 12(b) were acquired with a beam current of 1.6 nA and consequently a larger probe, from the same wall on the same sample as the data in Fig. 12(a). These two measurements were taken within 2 h of each other during a single data-acquisition run. As this electron probe distribution may change with the objective-lens focus, as described in Sec. II A, the upper and lower solid curves represent the two limiting values of the surface magnetization distribution obtained by convolving the calculated surface magnetization distribution with the 0.165- and 0.210-μm probes of Figs. 3(b) and 3(c), respectively. Within this range of focus we expect, the agreement is excellent.

In Fig. 12(c) we show the data of Oepen and Kirschner.[53] The incident-beam diameter for their measurements was less than 30 nm; hence we compare their data to the results of the unconvolved micromagnetic theory [Fig. 8(a)]. Again, the agreement remains excellent. A discussion of the statistical significance of the data will be given in Sec. IV C.

We can measure the surface-domain-wall offset Δ_{wall} from the SEMPA images such as those given in Figs. 2(a) and 2(b). The wall offset was defined as the distance between the peak in the bulk-Bloch-wall magnetization profile and the peak in the surface-Néel-wall profile as shown in Figs. 8(a) and 8(b). When the Bloch wall turns over at the surface, forming a surface Néel wall, the surface wall can fall to either side of the bulk Bloch wall. In the case where the surface wall is observed to fall on both sides of the same bulk Bloch wall, as it does in Fig. 2(a), the wall offset can be measured as twice the distance between the peaks in the surface-domain-wall magnetization profiles. We have measured this distance from data acquired with a probe FWHM of 0.070 μm. We determined the wall offset to be $\Delta_{\text{wall}}=0.047\pm0.008$ μm. The uncertainty in this measurement corresponds to $\frac{1}{2}$ of a pixel width (0.016 μm/pixel) in the raw data. The micromagnetic simulations predict a value of $\Delta_{\text{wall}}=0.050\pm0.008$ μm.

B. 180° surface domain walls in thin Permalloy films

Permalloy test samples were selected because its magnetic properties are extremely well characterized and, in contrast to Fe, has an extremely small magnetocrystalline anisotropy. This makes Permalloy a good test sample for investigating domain walls in magnetically soft materials. The Permalloy films were prepared by sputtering in a rf sputtering system employing an Ar plasma. The background pressure was 1×10^{-7} torr and the partial pressure of Ar was 3×10^{-6} torr for the 2-keV Ar plasma production. The sputter target was a cast Permalloy target, and the substrate was a crystal of Si. The Permalloy composition was $Ni_{0.81}Fe_{0.19}$. We show results for four Permalloy films of nominal thicknesses of 0.12, 0.16, 0.20, and 0.24 μm. The thickness of the three thinnest films were measured by x-ray fluorescence. The actual film thicknesses were 0.126 ± 0.003, 0.157 ± 0.004, and 0.193 ± 0.005 μm. The thickest film was measured with a stylus thickness device with a 2-μm stylus. The thickness of the thickest film was 0.242 ± 0.006 μm. These films were prepared for SEMPA observation using by 2-keV argon-ion sputtering, until the Auger electron signal from adsorbed carbon (285 eV) and the native oxide (535 eV) were gone. After the films were sputtered, they were observed with SEMPA. No annealing was performed. The thickness of the Permalloy films was reduced by roughly 0.005 ± 0.002 μm. The final thicknesses are 0.121 ± 0.004, 0.152 ± 0.004, 0.189 ± 0.005, and 0.237 ± 0.006 μm. The effect of the variation in thickness on the surface-domain-wall profiles for asymmetric Bloch walls in Permalloy films were already discussed.

In Figs. 13–16 we present the measured and calculated wall profiles for the four film thicknesses of Permalloy. We will refer to the films by their nominal film thicknesses, i.e., 0.12, 0.16, 0.20, and 0.24 μm. The data for 180° surface domain walls in a 0.120-μm-thick Permalloy film are shown in Figs. 13(a) and 13(b). In Fig. 13(a) the data were acquired with an incident-beam current of $I=0.3$ nA and a nominal probe diameter of 0.07 μm. In order to show how the measurements and predictions agree, taking into account our uncertainty in the probe diameter due to focusing, we show two limiting convolutions of the theory that we feel represent limiting cases. The upper solid line in the figure is the unconvolved result from the micromagnetic calculation. The lower solid curve is the same result after convolution with the probe-intensity profile of Fig. 3(a). In Fig. 13(b) the data were acquired with an incident-beam current of $I=1.6$ nA and a nominal probe diameter of 0.165–0.210 μm. The upper solid line in the figure is the result from the micromagnetic calculation convolved with the 0.165-μm limiting probe. The lower solid curve is the calculated result after convolution with the 0.210-μm probe-intensity profile of Fig. 3(c). This description of Fig. 13 is

summarized in Table I, and the corresponding data for the other three film thicknesses are shown in Figs. 14–16. The probe diameters used in the convolutions are also listed in Table I.

The qualitative agreement between each of the experimental and calculated domain-wall profiles is evident in Figs. 12–16. Furthermore, the measured and calculated profiles for the thin Permalloy films are both functions of the thickness of the film. A quantitative analysis of this data will be delayed until Sec. IV C.

1. Magneto-optic Kerr microscopy of a thin Permalloy film

We have made additional measurements of domain-wall profiles in Permalloy thin films using (longitudinal) magneto-optic Kerr microscopy. In magneto-optic Kerr microscopy, a polarized light beam incident through a light microscope objective lens upon a magnetized sample will be rotated upon reflection. The rotation in the polarization can be directly related to the sample magnetization. As an optical technique, the transverse spatial reso-

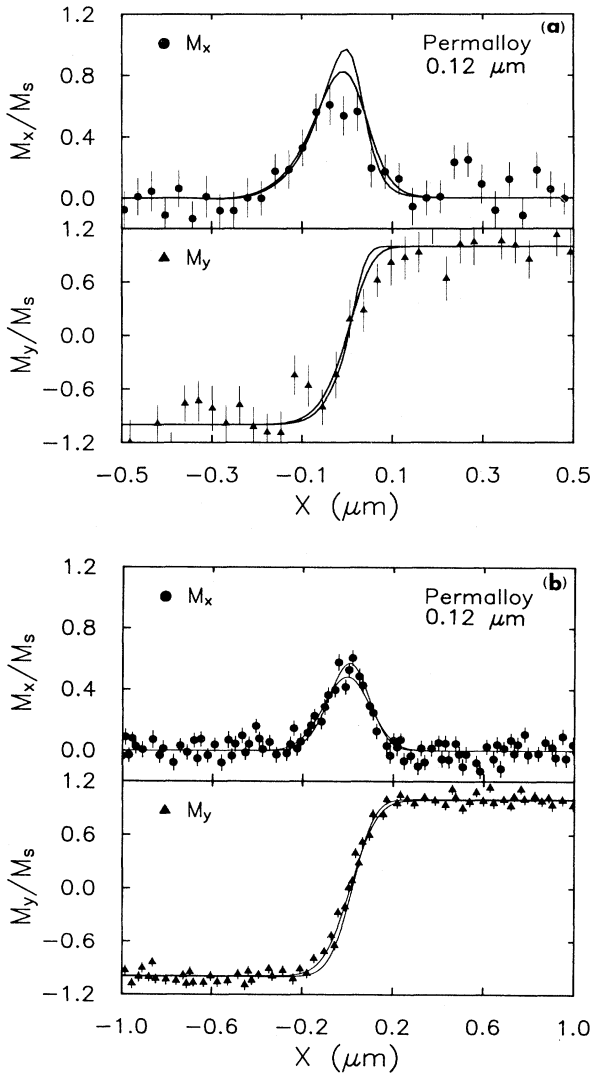

FIG. 13. (a) magnetization profiles for a 180° surface domain wall in a 0.12-μm-thick Permalloy film. The data were acquired with $I=0.3$ nA, and the solid lines are the raw result of micromagnetic theory (upper curve) and the theory convolved with the probe-intensity distribution of Fig. 3(a) (lower curve). (b) Magnetization profiles for a 180° surface domain wall in a 0.12-μm-thick Permalloy film. The data were acquired with $I=1.6$ nA, and the solid lines are the results of micromagnetic theory convolved with the limiting probe-intensity distributions of Fig. 3(c), FWHM=0.165 μm (upper curve) and 0.210 μm (lower curve).

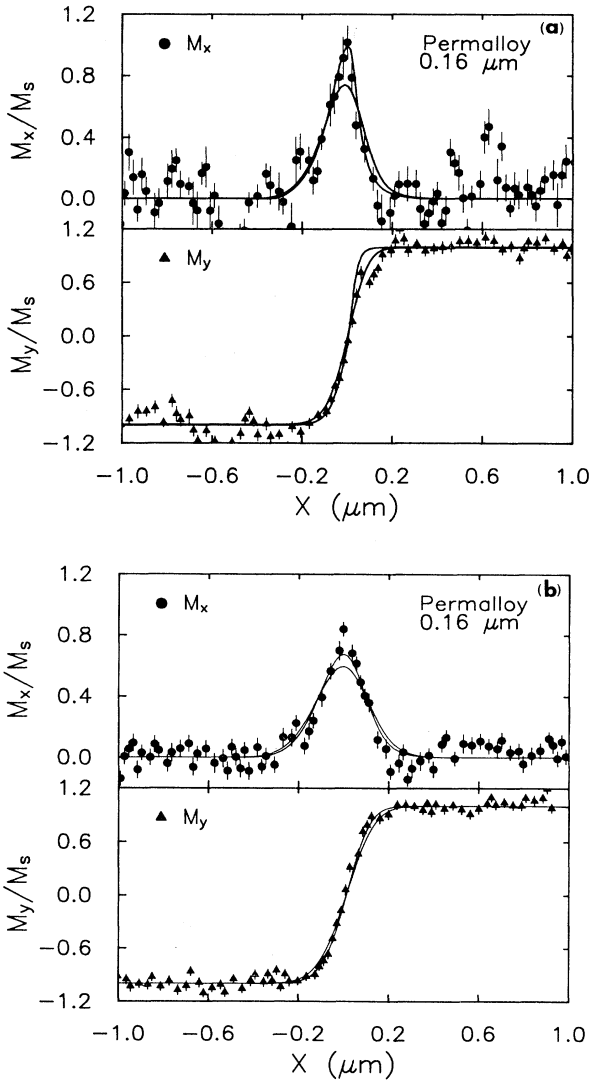

FIG. 14. (a) Magnetization profiles for a 180° surface domain wall in a 0.16-μm-thick Permalloy film. The data were acquired with $I=0.6$ nA, and the solid lines are the raw result of micromagnetic theory (upper curve) and the theory convolved with the probe-intensity distribution of Fig. 3(b) (lower curve). (b) Magnetization profiles for a 180° surface domain wall in a 0.16-μm-thick Permalloy film. The data were acquired with $I=1.6$ nA, and the solid lines are the results of micromagnetic theory convolved with the limiting probe-intensity distributions of Fig. 3(c), FWHM=0.165 μm (upper curve) and 0.210 μm (lower curve).

lution of magneto-optic Kerr microscopy is limited by diffraction to 0.25 μm. The depth resolution of the Kerr effect can be given by the attenuation length for light penetration into the ferromagnet. Typically, attenuation lengths are in the 10-nm range. This attenuation length is 3–10 times larger than that in SEMPA. We measured domain-wall profiles at surfaces using both SEMPA and magneto-optic Kerr microscopy to see if we could differentiate between the depth sensitivity of the two techniques and to identify if there is some special magnetic structure which is very localized to the surface.[55–60]

We measured surface domain walls in the same 0.24-μm-thick Permalloy film that was used for the SEMPA measurements. We carefully characterized the instrument transfer function of the Kerr microscope. We found that when we convolved the calculated magnetization profile with the Kerr instrument transfer function,

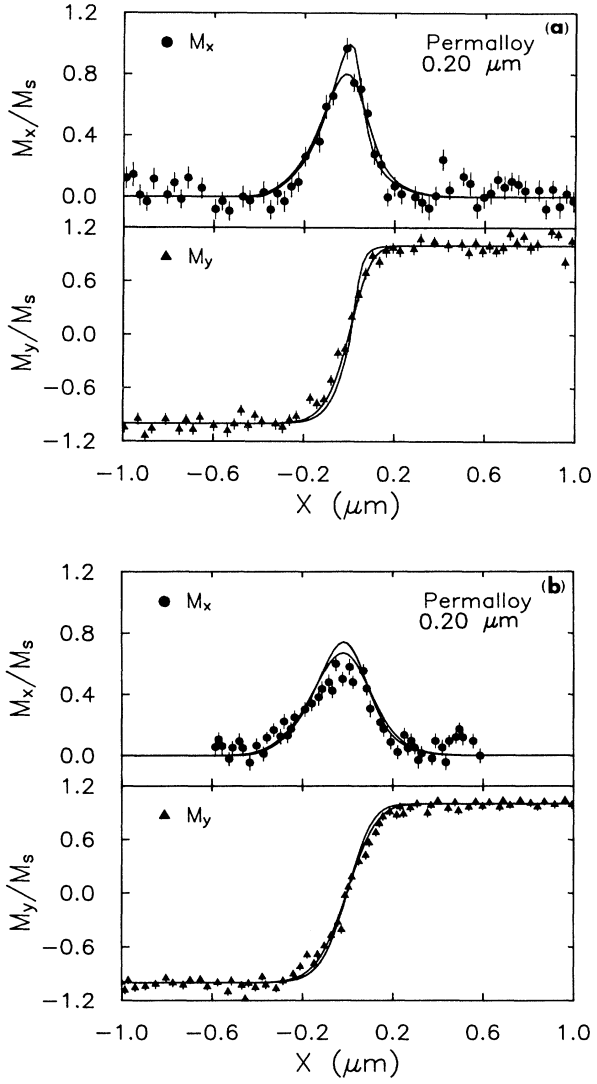

FIG. 15. (a) Magnetization profiles for a 180° surface domain wall in a 0.20-μm-thick Permalloy film. The data were acquired with I=0.6 nA, and the solid lines are the raw result of micromagnetic theory (upper curve) and the theory convolved with the probe-intensity distribution of Fig. 3(b) (lower curve). (b) Magnetization profiles for a 180° surface domain wall in a 0.20-μm-thick Permalloy film. The data were acquired with I=1.6 nA, and the solid lines are the results of micromagnetic theory convolved with the limiting probe-intensity distributions of Fig. 3(C), FWHM=0.165 μm (upper curve) and 0.210 μm (lower curve).

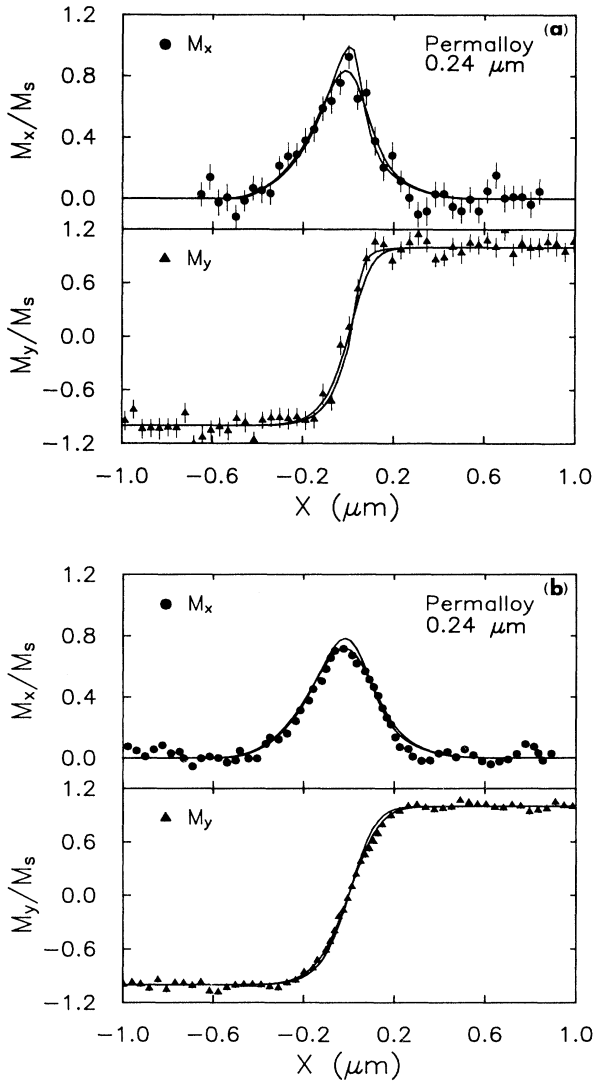

FIG. 16. (a) Magnetization profiles for a 180° surface domain wall in a 0.24-μm-thick Permalloy film. The data were acquired with I=0.6 nA, and the solid lines are the raw result of micromagnetic theory (upper curve) and the theory convolved with the probe-intensity distribution of Fig. 3(b) (lower curve). (b) Magnetization profiles for a 180° surface domain wall in a 0.24-μm-thick Permalloy film. The data were acquired with I=1.6 nA, and the solid lines are the results of micromagnetic theory convolved with the limiting probe-intensity distributions of Fig. 3(c), FWHM=0.165 μm (upper curve) and 0.210 μm (lower curve).

TABLE I. Summary of the domain-wall measurements, listing the ferromagnetic material, its thickness, the electron-probe current used for the measurement, the relevant figure number where the data is presented, the size of the beam probe for the theoretically convoluted curves, and the corresponding curve position in the figure.

Material	Thickness (μm)	Beam current I (nA)	Figure	Convolved probe diameter (μm)	Solid curve
Fe	20.0	0.3	12(a)	0.070	only curve
Fe	20.0	1.6	12(b)	0.165	upper curve
				0.210	lower curve
Fe (Ref. 53)			12(c)	0.000	only curve
Permalloy	0.12	0.3	13(a)	0.000	upper curve
				0.070	lower curve
Permalloy	0.12	1.6	13(b)	0.165	upper curve
				0.210	lower curve
Permalloy	0.16	0.6	14(a)	0.000	upper curve
				0.120	lower curve
Permalloy	0.16	1.6	14(b)	0.165	upper curve
				0.210	lower curve
Permalloy	0.20	0.6	15(a)	0.000	upper curve
				0.120	lower curve
Permalloy	0.20	1.6	15(b)	0.165	upper curve
				0.210	lower curve
Permalloy	0.24	0.6	16(a)	0.000	upper curve
				0.120	lower curve
Permalloy	0.24	1.6	16(b)	0.165	upper curve
				0.210	lower curve

the measured Kerr profile closely resembled the results of Fig. 16. We conclude that there is no difference between these surface-domain-wall profiles measured by SEMPA and Kerr except that the SEMPA measurements have much higher spatial resolution. This result verifies that the magnetic length scales at surfaces for domain walls are on the order of tens of nanometers [see Fig. 10(a)] and not on the order of angstroms or nanometers. The details of the Kerr measurements will be reported elsewhere.

C. Data analysis

1. Sources of error and error estimation

We have displayed excellent qualitative agreement between measured and calculated domain-wall profiles at surfaces. In our simulations we used only bulk parameters and did not include any special surface effects such as surface anisotropy or enhanced moments at the surface. We would like to examine the agreement between the measurements and calculations quantitatively to determine if such surface effects could greatly enhance the models. We begin the data analysis with a discussion of the experimental errors.

The error bars present on the data in Figs. 12–16 represent the standard deviation about the same value for the magnetization. The magnetization is the average value measured at each x position in multiple line scans. No other errors have been incorporated into these error bars.

The distance scale errors were found to be less than 2.0% from the measurement of a calibrated grid. Absolute scale errors, and errors introduced as a result of image rotation, to ensure that the wall magnetization components lay along the polarization detector axes, appear as scale corrections to the distance scale. The total adjustment to the distance scale across the width of a wall is always less than ± 0.007 μm due to wall misalignment. The M_x and M_y magnetization profiles are absolutely registered with respect to one another for both the experimental and calculated results. The experimental curves were aligned with the calculated curves by matching the zero crossing in the M_y profile. Since both the calculated and experimental M_y magnetization profiles have a steep slope near $M_y=0$, alignment to a fraction of a pixel width was possible.

The saturation magnetization was determined by averaging the magnitude of the magnetization over the entire image. The magnitude image is formed pixel by pixel as $|M|=(M_x^2+M_{y2})^{1/2}$. The same saturation magnetization value was used to normalize both the M_x and M_y magnetization profiles. The error in the determination of the saturation magnetization was a function of the incident-beam current, the intrinsic spin polarization of the material being analyzed, and the number of data points in the region being analyzed. The errors in determining this value were computed from the histogram of the magnetization values from an image, and the results are given in Table II.

The error limits in the micromagnetics simulations were estimated in Secs. III B 1 and III B 2. We allowed for variation in the values of the bulk magnetic parameters which entered into the calculations and the thickness uncertainty for the Permalloy thin films. We found that

TABLE II. Deviation in the measurement of the saturation magnetization for all of the data taken with different electron-probe currents.

Material	Thickness (μm)	Beam current I (nA)	$\Delta M_s/M_s$ (%)
Fe	20.0	0.3	±2.5
Fe	20.0	1.6	±1.3
Permalloy	0.12	0.3	±3.0
Permalloy	0.12	1.6	±1.8
Permalloy	0.16	0.6	±1.1
Permalloy	0.16	1.6	±1.4
Permalloy	0.20	0.6	±2.2
Permalloy	0.20	1.6	±1.4
Permalloy	0.24	0.6	±1.9
Permalloy	0.24	1.6	±1.0

the maximum deviation of the surface magnetization profile, due to the variation in magnetic parameters, was ±5.0%, averaging ±2.0% over the whole profile. We also found that errors introduced by the grid density and discretization region could introduce maximum deviations of ±5.0%, averaging ±2.0% over the whole profile. We calculate the total average variation due to errors in the modeling by adding these two contributions in quadrature, yielding an average error of ±2.8%. We choose this very pessimistic value of the error due to uncertainty in the parameters and grid in the modeling of 2.8%.

2. *Statistical measures of agreement between measurements and calculations*

Here we compare how well our theoretical model agrees with the data. For each value of position x_i, let the average magnetization measured along a profile be y_i. At x_i, let the model prediction be y_i^*. We write

$$y_i = y_i^* + \epsilon_i \quad (\text{for } i = 1,2,\ldots,N) , \tag{9}$$

where ϵ_i is the ith residual and N is the total number of points in the domain-wall magnetization profile. When the residuals are small, the agreement between the model and experimental data is good.

One statistical test for the agreement between a model and experiment is the χ^2 test. The chi-squared statistic χ_r^2 is defined as follows:

$$\chi_r^2 = \frac{1}{N-1} \sum_{i=1}^{N} \left[\frac{1}{\sigma_i^2} (y_i - y_i^*)^2 \right] , \tag{10}$$

where σ_i^2 is the estimated variance of the measured data at x_i. If the model exactly predicts the "infinite-data" experimental result, the chi-square statistic is one. When χ_r^2 is large, we reject the hypothesis that the model exactly predicts what would be observed if an infinite amount of data were taken. However, the χ_r^2 statistic can be large even if the difference between the model and infinite-data experimental result is very small. For example, if the errors in the data are small, but there exists one data point which anomalously lies far from the model curve, the chi-square statistic will be large. That is, the χ_r^2 statistic is a narrow test to determine if a model exactly fits the data. Additionally, if measurement errors are large, i.e., σ_i^2 is high, χ_r^2 can be low, even though the model may disagree with the measured data. Thus χ_r^2 is an ambiguous statistic.

In contrast to the chi-squared statistic, we compute a statistic R^2 which measures how much of the variability of the data is predicted by the model. R^2 is an index of the correlation.[87] To compute R^2 we must compare root-mean-square (rms) deviations to the variance of the data σ_{dat}^2 where

$$\sigma_{\text{dat}}^2 = \frac{1}{N-1} \sum_{i=1}^{N} (y_i - \langle y \rangle)^2, \langle y \rangle = \frac{1}{N} \sum_{i=1}^{N} y_i . \tag{11}$$

R^2 is defined to be the fraction of the variance of the data explained by the theory, i.e., how well the theory predicts the shape of the profiles in this case. Thus

$$R^2 = 1 - \sigma_{\text{th}}^2 / \sigma_{\text{dat}}^2 , \tag{12}$$

where

$$\sigma_{\text{th}}^2 = \frac{1}{N-1} \sum_{i=1}^{N} (y_i - y_i^*)^2 ,$$

and $R^2 = 1$ implies excellent correlation between the theoretical model and measurements.

In Tables III and IV we summarize the results of analyzing our Fe and Permalloy data with respect to the statistical measures just described. In all cases we limited the comparisons to the regions within the wall magnetization profile. In Tables III and IV we list the number of points in the wall profile itself, N, the rms deviation σ_{th}, the χ_r^2 and R^2 statistics. We differentiate the separate data sets by the beam current used for the data acquisition. Separate entries are given for the M_x and M_y magnetization distributions, as well as comparisons to each of the model calculations which were convolved with incident probe-intensity distributions, identified by the FWHM, for each of Figs. 12–16.

In the presence of sampling errors, if the same experiment were repeated and the same amount of data were collected, the new values of R^2 and σ_{th} would surely differ from what was computed in Tables III and IV. To study how random sampling errors affect the precision of our estimates for R^2 and σ_{th}, we estimated confidence intervals for both statistics using a bootstrap model.[88] At each value of x_i, a bootstrap replication of y_i is simulated. The kth bootstrap replication of y_i is $y_i^{(k)}$, where

$$y_i^{(k)} = y_i + \epsilon_i^{(k)} , \tag{13}$$

and $\epsilon_i^{(k)}$ is a random Gaussian with mean zero and variance equal to σ_i^2 (the variance of y_i that we compute from the line-scan data).

For the kth bootstrap replication, root-mean-square error is

$$(\sigma_{\text{th}})^{(k)} = \left[\frac{1}{N} \sum_{i=1}^{N} (y_i^* - y_i^{(k)})^2 \right]^{1/2} . \tag{14}$$

However, $(\sigma_{\text{th}})^{(k)}$ as defined is biased high. To correct for the bias, we subtract as follows:

TABLE III. Summary of the data for Fe at various incident electron-probe currents for both components M_x and M_y of the domain wall. N is the number of points in the profile, σ_{th} is the mean root-mean-square deviation, and χ_r is the reduced chi-square and R^2 is the r square correlations between the measurement and theoretical profiles (convoluted with the measured probe function).

N	Beam current (nA)	Component	Probe size (μm)	σ_{th}	χ_r^2	R^2
15	0.3	M_x	0.070	0.128	1.047	0.732
		M_y	0.070	0.089	0.623	0.986
18	Ref. 53	M_x	0.000	0.161	1.995	0.804
		M_y	0.000	0.168	2.192	0.943
30	1.6	M_x	0.165	0.096	5.026	0.584
			0.210	0.078	3.336	0.727
		M_y	0.165	0.102	3.390	0.977
			0.210	0.068	2.472	0.990

TABLE IV. Summary of the data for Permalloy at various incident electron-probe currents and film thickness for both components M_x and M_y of the domain wall. N is the number of points in the profile, σ_{th} is the mean root-mean-square deviation, and χ_r is the reduced chi-square and R^2 is the r-square correlations between the measurement and theoretical profiles (convoluted with the measured probe function).

N	Thickness (μm)	Beam current (nA)	Component	Probe size (μm)	σ_{th}	χ_r^2	R^2
16	0.12	0.3	M_x	0.000	0.134	1.339	0.686
				0.065	0.100	0.735	0.823
			M_y	0.000	0.364	2.462	0.776
				0.065	0.332	2.039	0.814
46	0.12	1.6	M_x	0.165	0.057	1.353	0.918
				0.210	0.075	2.447	0.859
			M_y	0.165	0.095	3.455	0.987
				0.210	0.067	1.667	0.993
13	0.16	0.6	M_x	0.000	0.107	3.543	0.897
				0.120	0.158	7.078	0.775
			M_y	0.000	0.159	15.842	0.956
				0.120	0.107	7.468	0.980
37	0.16	1.6	M_x	0.165	0.093	3.295	0.882
				0.210	0.119	5.412	0.809
			M_y	0.165	0.071	2.160	0.993
				0.210	0.094	3.542	0.987
23	0.20	0.6	M_x	0.000	0.078	1.408	0.934
				0.120	0.093	2.155	0.905
			M_y	0.000	0.127	4.468	0.975
				0.120	0.078	1.610	0.991
60	0.20	1.6	M_x	0.165	0.087	3.422	0.778
				0.210	0.076	2.602	0.834
			M_y	0.165	0.092	5.243	0.988
				0.210	0.072	3.242	0.992
24	0.24	0.6	M_x	0.000	0.086	1.176	0.914
				0.120	0.079	0.961	0.929
			M_y	0.000	0.106	0.923	0.986
				0.120	0.117	1.191	0.982
58	0.24	1.6	M_x	0.165	0.041	4.594	0.964
				0.210	0.045	5.483	0.958
			M_y	0.165	0.053	4.629	0.992
				0.210	0.028	1.244	0.997

TABLE V. Summary of the sensitivity analysis for the Fe data at various incident electron-probe currents for both components M_x and M_y of the domain wall. σ_{th} is the mean root-mean-square deviation, and R^2 is the r-square correlation between the measurement and theoretical profiles (convoluted with the measured probe function). The (5%) and (95%) confidence intervals for these statistics are given.

Beam current (na)	Component	Probe size (μm)	σ_{th} (5%)	σ_{th} (95%)	R^2 (5%)	R^2 (95%)
0.3	M_x	0.070	0.040	0.187	0.982	0.512
	M_y	0.070	0.026	0.145	0.999	0.964
Ref. 53	M_x	0.000	0.100	0.204	0.924	0.734
	M_y	0.000	0.113	0.212	0.978	0.912
1.6	M_x	0.165	0.081	0.108	0.742	0.487
		0.210	0.063	0.090	0.833	0.673
	M_y	0.165	0.088	0.114	0.985	0.973
		0.210	0.051	0.081	0.995	0.987

TABLE VI. Summary of the sensitivity analysis for the Permalloy data at various incident electron-probe currents for various film thicknesses for both components M_x and M_y of the domain wall. σ_{th} is the mean root-mean-square deviation, and R^2 is the r-square correlation between the measurement and the theoretical profiles (convoluted with the measured probe function). The (5%) and (95%) confidence intervals for these statistics are given.

Thickness (μm)	Beam current (nA)	Component	Probe size (μm)	σ_{th} (5%)	σ_{th} (95%)	R^2 (5%)	R^2 (95%)
0.12	0.3	M_x	0.000	0.059	0.183	0.955	0.514
			0.065	0.026	0.156	0.990	0.686
		M_y	0.000	0.246	0.469	0.912	0.664
			0.065	0.207	0.437	0.938	0.715
0.12	1.6	M_x	0.165	0.042	0.071	0.958	0.884
			0.210	0.061	0.087	0.980	0.833
		M_y	0.165	0.081	0.107	0.991	0.983
			0.210	0.052	0.080	0.996	0.991
0.16	0.6	M_x	0.000	0.066	0.137	0.964	0.846
			0.120	0.124	0.188	0.864	0.744
		M_y	0.000	0.138	0.177	0.971	0.950
			0.120	0.086	0.124	0.989	0.976
0.16	1.6	M_x	0.165	0.077	0.107	0.920	0.859
			0.210	0.104	0.133	0.853	0.789
		M_y	0.165	0.055	0.085	0.996	0.990
			0.210	0.077	0.107	0.992	0.984
0.20	0.6	M_x	0.000	0.047	0.100	0.979	0.897
			0.120	0.064	0.117	0.955	0.875
		M_y	0.000	0.103	0.146	0.985	0.968
			0.120	0.050	0.990	0.997	0.986
0.20	1.6	M_x	0.165	0.076	0.097	0.852	0.731
			0.210	0.063	0.086	0.895	0.793
		M_y	0.165	0.083	0.101	0.991	0.986
			0.210	0.062	0.081	0.995	0.991
0.24	0.6	M_x	0.000	0.031	0.109	0.990	0.888
			0.120	0.045	0.147	0.998	0.975
		M_y	0.000	0.064	0.157	0.995	0.971
			0.120	0.047	0.056	0.965	0.950
0.24	1.6	M_x	0.165	0.034	0.047	0.977	0.955
			0.210	0.038	0.051	0.977	0.950
		M_y	0.165	0.044	0.061	0.996	0.991
			0.210	0.017	0.036	1.000	0.997

$$(\sigma_{\rm th})_c^{(k)} = \left[[(\Delta y)^{(k)}]^2 - \frac{1}{N} \sum_{i=1}^{N} \sigma_i^2 \right]^{1/2} . \quad (15)$$

The corrected root-mean-square deviation $(\sigma_{\rm th})_c^{(k)}$ is not biased. By a similar method the variance of the kth bootstrap replication of the data $\sigma_{\rm dat}^{(k)2}$ is corrected for bias.

As a caveat, we did not incorporate the variability in M_s into our bootstrap analysis. That is, we are studying the effects of random sampling errors on $\sigma_{\rm th}$ and R^2 assuming that M_s is well determined. In fact, according to Table II, M_s is well determined to within a percent or two for most cases. Hence, if this variability could be incorporated, the resultant confidence intervals for $\sigma_{\rm th}$ and R^2 would be slightly broader.

In Tables V and VI we present the results of this sensitivity analysis and give confidence intervals for $\sigma_{\rm th}(5\%,95\%)$ and $\sigma_{\rm th}(5\%,95\%)$. The confidence interval indicates, for example, that the rms deviation of data, as simulated with some given statistical variation, will agree with a particular model within a $\sigma_{\rm th}$ given by the 5% confidence value only 5% of the time, whereas the $\sigma_{\rm th}$ will be within the 95% confidence value 95% of the time. A 95% $\theta_{\rm th}$ confidence interval can serve as a conservative estimate of the deviation of the data.

To illustrate how to interpret the information in Tables III–VI, we examine the M_x profile taken with 1.6 nA of current and a probe of 0.210 μm from Table III. We see that the rms deviation of the data from the model is 0.078. The corresponding confidence intervals given in Table V show that $\sigma_{\rm th}(5\%)=0.063$ and $\sigma_{\rm th}(95\%)=0.090$. Thus we see that the rms values simulated from the data using the bootstrap algorithm are tightly distributed about the measured rms value, as it should be given the relatively small error bars on the data. We can see that although our data had an rms deviation of 0.078, a pessimistic value of the rms deviation (worst case essentially) for data with statistics such as ours will only be 0.090. We emphasize how conservative this estimate is by noting that the 95% confidence intervals is equivalent to setting error bars between two and three standard deviations.

The data in Figs. 12–15 indicate a clear qualitative agreement between the SEMPA measurements of surface-domain-wall profiles and the results of micromagnetic theory using only bulk parameters. For most measurements the χ^2 statistic for the deviation between the experimental and calculated domain-wall profiles was between 1 and 2, as indicated in Tables III and IV. This indicates that the agreement between the model and measurements is statistically significant. The R^2 statistic for the deviation between the model and measurements was mostly between 0.8 and 1. This indicates that the model predicts the variability in the data accurately.

We summarize the results for Fe by concluding that the total root-mean-square deviation of the measurements from the model calculation is about 0.109 for our high-resolution, low-current measurements, and about 0.073 for the high-current measurements, where in each case we have just averaged $\sigma_{\rm th}$ for M_x and M_y in Table III. The high-current measurements rely on knowing the details of the probe-intensity distribution. Pessimistic values for the rms deviation for this data, as derived from our sensitivity analysis, are given by the 95% confidence level in the rms values. The maximum rms deviations are 0.187 and 0.108 for the low- and high-current cases, respectively, as found in Table V.

The results for the Permalloy (Table IV) are very similar to those of the Fe. The rms deviation for the measurements from the model calculations ranges between about 0.10 and 0.125 for low-current measurements, and between 0.05 and 0.09 for the high-current measurements. Once again, the high-current measurements rely implicitly on the confidence in assessing the probe-intensity distribution. Pessimistic values for the rms deviation for this data as derived from our sensitivity

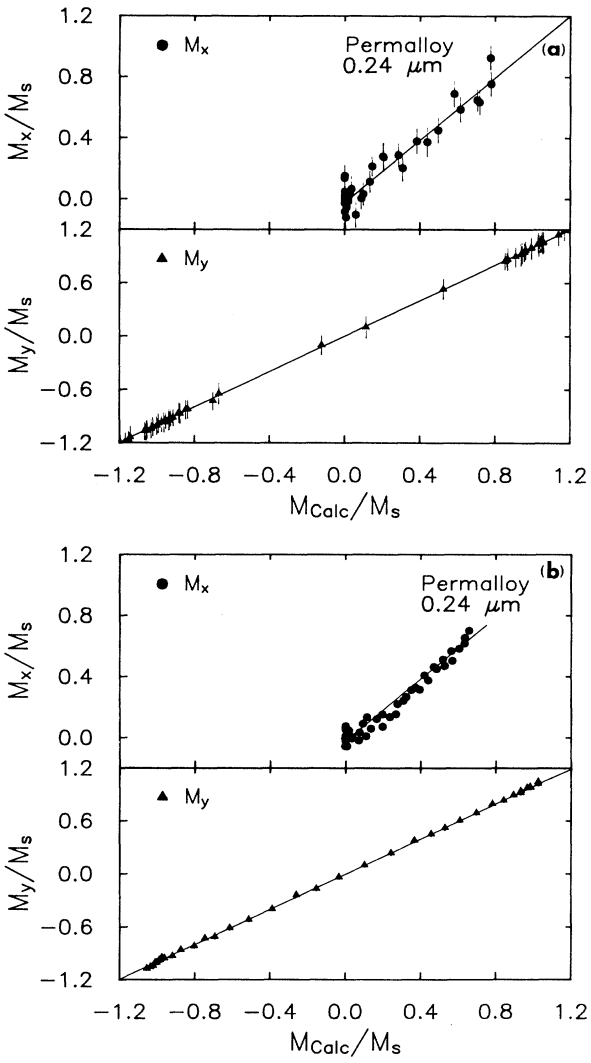

FIG. 17. (a) Permalloy data of Fig. 16(a) plotted vs the calculated magnetization convolved with the 0.110-μm probe [lower solid curve in Fig. 16(a)]. A line-of-unity slope shown in the figure indicates perfect agreement. (b) Permalloy data of Fig. 16(b) plotted vs the calculated magnetization convolved with the 0.210-μm probe [lower solid curve in Fig. 16(b)].

analysis (Table VI) given by rms range between 0.05 and 0.10. The low-current measurements of the 0.12-μm-thick Permally film are likely at the edge of our spatial resolution capabilities.

We tested the micromagnetic model for the additional effects of surface anisotropy. We found in Fe, for example, that a surface anisotropy[80] as high as 5.0 erg/cm^2 produced rms deviations in the surface-domain-wall magnetization profile of less than 0.01 from that calculated without surface anisotropy. We therefore cannot experimentally identify the significance of the role of surface anisotropy in surface-domain-wall structure with our data at the current signal-to-noise level. We note further that the rms deviations in the surface-domain-wall profile due to surface anisotropy are still less than those deviations produced by varying the input parameters by $\pm 5.0\%$. We conclude that the magnetic parameters will additionally have to be known to much higher precision before surface anisotropy effects on surface domain walls can be investigated.

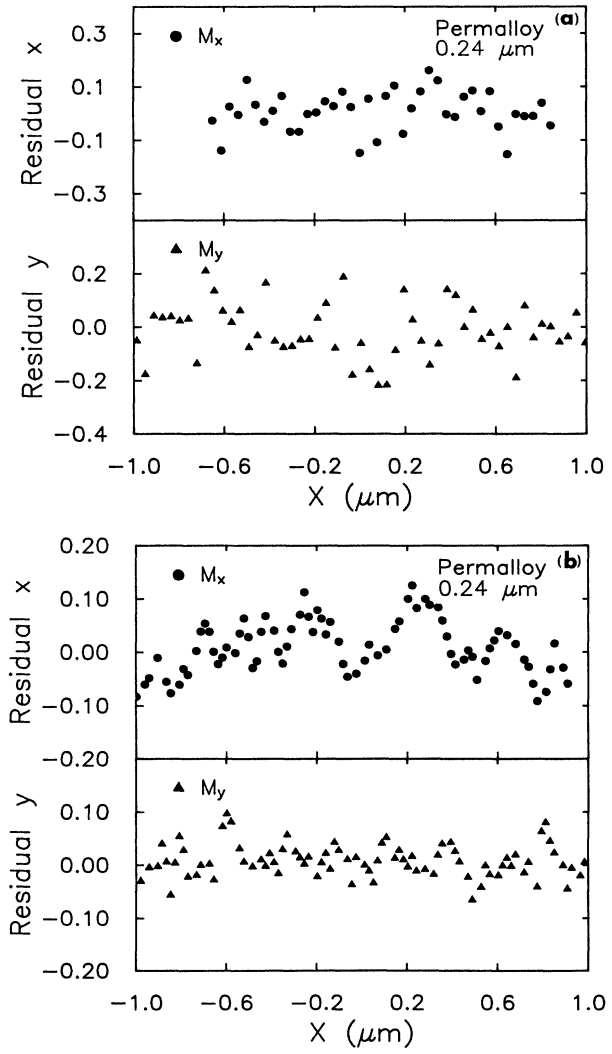

FIG. 18. Residuals of the data from the calculated profiles (lower curves) for the data of (a) Fig. 16(a) and (b) Fig. 16(b), respectively.

We present our data in two additional formats to illustrate the agreement between the model calculations and measurements. In Figs. 17(a) and 17(b) we show the data for the 0.24-μm-thick Permalloy film acquired at $I=0.6$ and 1.6 nA, respectively. The experimental data are plotted on the vertical scale as a function of the calculated values of the horizontal scale. Perfect agreement would yield a straight line of slope 1 on each graph. Note that the graphs have different vertical scales which reflect the range of the magnetization values. The data are plotted versus the theory convolved with the 0.110-μm-diam probe in Fig. 17(a), and the theory convolved with the 0.210-μm-diam probe in Fig. 17(b). The solid straight line is for perfect agreement. The agreement between the model calculations and data are nicely displayed in this format.

Finally, we search for patterns in the difference between the model and measurements. The residuals, i.e., ϵ_i, for data from the 0.24-μm-thick Permalloy film for $I=0.6$ and 1.6 nA, are plotted in Figs. 18(a) and 18(b), respectively. Interestingly, we can identify some correlation in the rms deviation structure, most evident in Fig. 18(b) as "bumps" in the M_x deviations near $x=0.2$ μm. By examining the original data in Fig. 16(b), we can see that the deviations result from the waviness near the edge of the domain wall. This waviness is present in several of the other data sets, but is most evident in Fig. 16(b). These waves are possibly the result of rippling[89] within the uniform domain adjacent to the domain wall. We would require very good statistics to analyze such small magnetization deviations systematically.

V. DISCUSSION

We have calculated and measured 180° surface-domain-wall profiles in Fe and Permalloy. The agreement between the micromagnetic simulations and measured profiles was quantitatively presented in Tables III–VI and Figs. 12–18. We find very good agreement using only bulk parameters in the calculations. An interesting question is whether the agreement can be improved by including explicitly surface parameters, for example, a surface anisotropy. As we pointed out, by including even a rather large surface anisotropy of 5 erg/cm^2 in the calculation for the Fe surface-domain-wall profile, the change in the rms deviation was less than 0.01. Basically, the surface anisotropy has only a very small influence on the surface-domain-wall profile. In fact, it is smaller than the present experimental uncertainty and the uncertainty in the simulation caused by the uncertainty in the input parameters.

These results indicate that bulk micromagnetic models accurately predict the behavior of the magnetization in a surface-domain-wall profile. The calculations further give a "window" on the magnetization distribution in the bulk which is not otherwise readily determined. In one case where some experimental data was available, we compared and found agreement between our micromagnetic simulations and "bulk" asymmetric Bloch-wall

widths measured by Lorentz microscopy for sufficiently thin Fe films.[70] Our micromagnetic calculations with periodic boundary conditions to simulate a bulk Bloch wall in an infinite sample were shown to agree well with the analytical solutions. For an infinite sample with cubic anisotropy, the calculated 180° wall was found to break into two 90° walls, as expected. Significantly, in a realistic sample with a surface, the magnetostatic energy at the surface was found to be sufficient, without introducing magnetostriction, to prevent the 180° wall from breaking up. The calculations showed that the width of a bulk Bloch wall is typically about half that of a surface Néel wall.

The understanding of the behavior of domain walls near the surface has interesting consequences for the observation of magnetic microstructure. By examining the cross-sectional view of the calculated domain walls for Fe and Permalloy shown in Figs. 5 and 10(a), respectively, we can see the depth which the surface domain wall penetrates into the bulk of the ferromagnet. For the thick-film (crystal) case depicted for Fe, the penetration depth is on the order of a Bloch-wall width. For thin films such as the case depicted for Permalloy, the penetration depth of the magnetic disturbance associated with the surface is limited by the film thickness. For films which are thinner than about three Bloch-wall widths, which leads to asymmetric Bloch walls, the penetration depth is about one-third of the film thickness. For films which are thicker than three Bloch-wall widths, the penetration into the bulk of the surface wall is fixed to roughly one Bloch-wall width and does not further increase with film thickness.[70] Because of this relatively large length scale over which changes in magnetic microstructure occur at the surface, there is no difference in a surface-domain-wall profile measured by SEMPA with a probing depth of about 1 nm and that measured with the magneto-optic Kerr effect with a probing depth of about 15 nm beyond, of course, the difference in lateral spatial resolution of the techniques. This has been confirmed experimentally in the observation of domain walls in thin Permalloy films.[90] For very "hard" magnetic materials, that is, with high anisotropy, the Bloch-wall width could be very narrow, and some differences between SEMPA and Kerr measurements would be expected owing to their different probing depths. However, a surface-domain-wall profile of such a material would be beyond the resolution of a Kerr measurement, and so, in practice, our assertion about the similarity of the results of the two techniques holds.

Whereas magnetic microstructure changes occur on a length scale of approximately a Bloch-wall width, we noted in the Introduction other measurements for which changes are observed in the outer atomic layer or two. This difference in length scale is a distinctive feature distinguishing surface magnetic microstructure from some other surface phenomena. The temperature dependence of surface magnetism is different from the bulk[55,56] because the spin waves giving rise to the low-temperature spin deviations have different boundary conditions at the surface. Also, there is the additional effect of a softened exchange coupling of the outer layer to the bulk.[57,58] Surface hysteresis curves different from the bulk have been attributed to domain nucleation sites in the surface layers.[59] Increased magnetic moments at the surface have as their origin the lower coordination of the outer layer of atoms.[60] Each of these effects is directly related to some differences in the outer atomic layer. In contrast, magnetic microstructure is influenced by the surface primarily through the long-ranged magnetostatic interaction and changes in domains, and domain walls take place over a longer length scale.

In summary, a quantitative comparison between surface-domain-wall profiles measured by SEMPA and calculated using bulk magnetic parameters has been presented. The excellent agreement gives us confidence in the calculations which have provided further insight into the transition of domain-wall structure that takes place between the surface and bulk.

ACKNOWLEDGMENTS

This research was supported in part by the Office of Naval Research. We wish to thank M. H. Kelley and R. Freemire for assistance with image processing. We would also like to thank Dr. R. Victora, Professor H. Seigmann, and Professor A. Aharoni for stimulating discussions. We also thank Professor A. Aharoni for providing results prior to publication. We thank A. Arrott for supplying the Fe whiskers, which were grown at Simon Fraser University, Burnaby, British Columbia under an operating grant from the Natural Sciences and Engineering Research Council of Canada.

APPENDIX

We include explicit expressions in this appendix for the energy and effective-field terms used in our micromagnetic simulations. The square discretized elements have edge length Δ, and the ordering scheme is shown in Fig. 4. The (nearest-neighbor) exchange energy is given by

$$E_{\rm ex}=2A\sum_{I=1}^{N_z+2}\sum_{J=1}^{N_x+1}[1-\boldsymbol{\alpha}(J,I)\cdot\boldsymbol{\alpha}(J+1,I)]+2A\sum_{I=2}^{N_z}\sum_{J=1}^{N_x+1}[1-\boldsymbol{\alpha}(J,I)\cdot\boldsymbol{\alpha}(J,I+1)]$$
$$+4A\sum_{J=1}^{N_x+1}[2-\alpha(J,1)\cdot\boldsymbol{\alpha}(J,2)-\alpha(J,N_z+1)\cdot\boldsymbol{\alpha}(J,N_z+2)]\ . \tag{A1}$$

In the absence of surface anisotropy, the last term would be 0, but in the presence of surface anisotropy $\mathbf{m}\times[\partial E_{ks}/\partial z-(2A/M_s)\partial\mathbf{M}/\partial z]=0$, and the last term in (A1) is nonvanishing. The effective magnetic field at location (J,I) due to exchange is given by the Laplacian for a square mesh as

$$\mathbf{H}_{ex}=[2A/M_s\Delta^2)]\{\mathbf{x}[\alpha(J+1,I)+\alpha(J-1,I)+\alpha(J,I+1)+\alpha(J,I-1)-4\alpha(J,I)] +\mathbf{z}[\gamma(J+1,I)+\gamma(J-1,I)+\gamma(J,I+1)+\gamma(J,I-1)-4\gamma(J,I)]\} \ . \tag{A2}$$

The magnetocrystalline anisotropy energies and effective fields for uniaxial symmetry (easy axis in $\mathbf{y}$) and cubic symmetry, respectively, are given by

$$E_{Ku}=\sum_{I=2}^{N_z+1}\sum_{J=2}^{N_x+1}\Delta^2\{K_{u1}[1-\beta(J,I)^2]+K_{u2}[1-\beta(J,I)^2]^2\} \ , \tag{A3}$$

$$\mathbf{H}_{Ku}=2K_{u1}(1/M_s)\mathbf{y}\beta(J,I)\{1+2(K_{u2}/K_{u1})[1-\beta(J,I)]\} \ , \tag{A4}$$

$$E_{Kc}=\sum_{I=2}^{N_z+1}\sum_{J=2}^{N_x+1}\Delta^2\{K_{c1}[\alpha(J,I)^2\beta(J,I)^2+\beta(J,I)^2\gamma(J,I)^2+\gamma(J,I)^2\alpha(J,I)^2]+K_{c2}\alpha(J,I)^2\beta(J,I)^2\gamma(J,I)^2\} \ , \tag{A5}$$

$$\mathbf{H}_{Kc}=-2K_{c1}(1/M_s)(\mathbf{x}\{\alpha(J,I)[\beta(J,I)^2+\gamma(J,I)^2+(K_{c2}/K_{c1})\beta(J,I)^2\gamma(J,I)^2]\} +\mathbf{y}\{\beta(J,I)[\alpha(J,I)^2+\gamma(J,I)^2+(K_{c2}/K_{c1})\alpha(J,I)^2\gamma(J,I)^2]\} +\mathbf{z}\{\gamma(J,I)[\alpha(J,I)^2+\beta(J,I)^2+(K_{c2}/K_{c1})\alpha(J,I)^2\beta(J,I)^2]\}) \ , \tag{A6}$$

$$E_{Ks}=\sum_{J=2}^{N_x+1}(K_{s1}\Delta/2)[\gamma(J,1)^2+\gamma(J,N_z+2)^2]+(K_{s2}\Delta/2)[\alpha(J,1)\beta(J,1)+\alpha(J,N_z+2)\beta(J,N_z+2)] \ , \tag{A7}$$

$$\mathbf{H}_{Ks}=-\mathbf{z}K_{s1}\gamma(J,I)/\Delta-(K_{s2}/2\Delta)[\mathbf{x}\beta(J,I)+\mathbf{y}\alpha(J,I)] \ . \tag{A8}$$

The effective fields for the surface anisotropy are evaluated at $I=2$ or N_z+2 only.

The expressions for the self-energy are derived from integrating the total energy due to all of the effective magnetic charges in the wall region. We use the formulation for the magnetostatic self-energy as derived by LaBonte.[11] The magnetostatic energy can be determined from the following expression:

$$E_s=\tfrac{1}{2}\int\rho_s\rho_f G(\mathbf{r}_f|\mathbf{r}_s)d\tau \ . \tag{A9}$$

The magnetic charge densities ρ_s and ρ_f result from a divergence in the magnetization at the source s and field f points, respectively. $G(\mathbf{r}_f|\mathbf{r}_s)$ is the Green's function for the scaler potential, which for our two-dimensional formulation is given by $-\ln(\mathbf{r}_f-\mathbf{r}_s)^2$. $d\tau$ is the infinitesimal volume of the appropriate dimension. The effective charge densities in this numerical formulation will be isolated at the boundaries of the magnetic elements of the grid in Fig. 4. This is a boundary element approach.

We will consider two separate formulations for the magnetic self-energy. The first formulation is applicable for systems where the boundary conditions have the magnetization oriented in the $\mathbf{y}$ direction and for films with two surfaces. In this "cubic" formulation, we determine the effective charges on the boundaries of each magnetic subelement in the grid. The magnetic charge is $\rho=\mathbf{M}\cdot\mathbf{n}$, where $\mathbf{n}$ is the outward facing normal of each cubic subelement. The energy can be expressed as a double sum over the grid subelements as follows:

$$E_s=\frac{M_s^2\Delta^2}{2}\sum_{I_f=2}^{N_z+1}\sum_{J_f=2}^{N_x+1}\sum_{I_s=2}^{N_z+1}\sum_{J_s=2}^{N_x+1}\{A(K,L)[\alpha(J_s,I_s)\alpha(J_f,I_f)-\gamma(J_s,I_s)\gamma(J_f,I_f)] +C(K,L)[\alpha(J_s,I_s)\gamma(J_f,I_f)-\gamma(J_s,I_s)\alpha(J_f,I_f)]\} \ . \tag{A10}$$

The coupling constants $A(K,L)$ and $C(K,L)$ originally given by LaBonte[11] are integrals over the Green's functions summed over all of the faces of the two cubes and depend only on the distance between the subelements in the grid, $K=J_s-J_f$ and $L=I_s-I_f$. The coupling coefficients are given explicitly as follows:[11]

$$A(K,L)=I_1(K-1,L-1)-2I_1(K,L-1)+I_1(K+1,L-1)-2I_1(K-1,L)+4I_1(K,L)-2I_1(K+1,L) +I_1(K-1,L+1)-2I_1(K,L+1)+I_1(K+1,L+1) \ , \tag{A11}$$

$$C(K,L)=I_2(K-1,L-1)-2I_2(K,L-1)+I_2(K+1,L-1)-2I_2(K-1,L)+4I_2(K,L)-2I_2(K+1,L) +I_2(K-1,L+1)-2I_2(K,L+1)+I_2(K+1,L+1) \ , \tag{A12}$$

$$I_1(K,L)=\tfrac{1}{2}(L^2-K^2)\ln(L^2+K^2)+2KL\tan^{-1}(L/K) \ , \tag{A13}$$

$$I_2(K,L)=KL\ln(L^2+K^2)+(K^2-L^2)\tan^{-1}(L/K) \ . \tag{A14}$$

It can be recognized that the integrals I_1 and I_2 (LaBonte's[11] G_1 and G_2) are symmetric and antisymmetric, respective-

ly, with respect to changing sign on K or L, that is, $A(K,L)=A(-K,L)=A(K,-L)=A(-K,-L)$ and $C(K,L)=-C(-K,L)=-C(K,-L)=C(-K,-L)$. The magnetostatic self-energy for a cell on itself can be determined by examining the coupling coefficients when K and L are zero. The self-energy of a single cell on itself is $\pi M_s^2\Delta^2(\alpha^2+\gamma^2)$. An alternative representation for this self-energy which incorporates the constraint equation $|\alpha(\mathbf{r})|=1$ is $\pi M_s^2\Delta^2(1-\beta^2)$. LaBonte[11] discusses the interpretation of these alternative representations, although the real effective fields for integrating the Landau-Lifshitz-Gilbert equation must be derived from the original energy expression $\pi M_s^2\Delta^2(\alpha^2+\gamma^2)$.

The effective fields resulting from the magnetostatic self-energy take the following form:

$$\mathbf{H}_s=-M_s\sum_{I=2}^{N_z+1}\sum_{J=2}^{N_x+1}\mathbf{x}[A(K,L)\alpha(J,I)+C(K,L)\gamma(J,I)]+\mathbf{z}[-A(K,L)\gamma(J,I)+C(K,L)\alpha(J,I)]\ . \tag{A15}$$

Alternatively, if the $I=J$ term is removed from the above sum, then an effective field in the **y** direction can be included in the energy minimization as

$$\mathbf{H}_s(\text{self})=2\pi M_s\mathbf{y}\beta(J,I)\ , \tag{A16}$$

where it is understood that this substitution is only appropriate for the energy-minimization method. It is attractive here because the energy-minimization problem becomes more stable numerically when formulated in this manner.

The second formulation for the magnetic self-energy can be used for cases where the boundary conditions force the magnetization to be along a direction other than along **y** and for cases where infinite or bounded crystals are to be examined. This is the "interface" formulation. Here we consider the source of the magnetic charge at the interfaces to be the difference in **M** between two neighboring subelements. Thus the charge on the interface between $\mathbf{M}(J,I)$ and $\mathbf{M}(J-1,I)$ is $\alpha_i(J,I)=\alpha(J,I)-\alpha(J-1,I)$. The expression for the self-energy in this formulation is given as

$$E_s=\frac{M_s^2\Delta^2}{2}\sum_{I_f=2}^{N_z+1}\sum_{J_f=2}^{N_x+1}\sum_{I_s=2}^{N_z+2}\sum_{J_s=2}^{N_x+2}\{A_x(K,L)\alpha_i(J_s,I_s)\alpha(J_f,I_f)+A_z(K,L)\gamma_i(J_s,I_s)\gamma(J_f,I_f)$$
$$+C_{xz}(K,L)\alpha_i(J_s,I_s)\gamma(J_s,I_s)\gamma(J_f,I_f)+C_{zx}(K,L)\gamma_i(J_s,I_s)\alpha(J_f,I_f)\}\ . \tag{A17}$$

The "interface" coupling coefficients are given explicitly as follows, where K and L are as defined above:

$$A_x(K,L)=-I_{1x}(K,L-1)+I_{1x}(K+1,L-1)+2I_{1x}(K,L)-2I_{1x}(K+1,L)-I_{1x}(K,L+1)+I_{1x}(K+1,L+1)\ , \tag{A18}$$

$$A_z(K,L)=-I_{1z}(K-1,L)+2I_{1z}(K,L)-I_{1z}(K+1,L)$$
$$+I_{1z}(K-1,L+1)-2I_{1z}(K,L+1)+I_{1z}(K+1,L+1)\ , \tag{A19}$$

$$C_{xz}(K,L)=-I_{2xz}(K-1,L)+2I_{2xz}(K,L)-I_{2xz}(K+1,L)$$
$$+I_{2xz}(K-1,L+1)-2I_{2xz}(K,L+1)+I_{2xz}(K+1,L+1)\ , \tag{A20}$$

$$C_{zx}(K,L)=-I_{2xz}(K,L-1)+I_{2xz}(K+1,L-1)+2I_{2xz}(K,L)-2I_{2xz}(K+1,L)-I_{2xz}(K,L+1)+I_{2xz}(K+1,L+1)\ , \tag{A21}$$

$$I_{1x}(K,L)=\tfrac{1}{2}(L^2-K^2)\ln(L^2+K^2)+2KL\tan^{-1}(L/K)-3L^2/2\ , \tag{A22}$$

$$I_{1z}(K,L)=\tfrac{1}{2}(K^2-L^2)\ln(L^2+K^2)+2KL\tan^{-1}(K/L)-3K^2/2\ , \tag{A23}$$

$$I_{2xz}(K,L)=KL\ln(L^2+K^2)+K^2\tan^{-1}(L/K)+L^2\tan^{-1}(K/L)-3KL\ . \tag{A24}$$

Special care should be taken at the surfaces for the periodic boundary condition case (where the top layer of pixels, $I=2$, is equated with the bottom layer of pixels, $I=N_z+1$, and no surface pixels, $I=1$, N_z+2, are allowed), where the contribution to the self-energy due to the top and bottom surfaces must to be subtracted. The effective magnetic field for this formulation is explicitly

$$\mathbf{H}_s=M_s\sum_{I=2}^{N_z+1}\sum_{J=2}^{N_x+1}\mathbf{x}[A_x(K,L)\alpha_i(J,I)+C_{zx}(K,L)\gamma_i(J,I)]+\mathbf{z}[A_z(K,L)\gamma_i(J,I)+C_{xz}(K,L)\alpha_i(J,I)]\ . \tag{A25}$$

Finally, the energy and effective-field contributions due to external fields $\mathbf{H}_0=(H_{0x},H_{0y},H_{0z})$ are given as

$$E_h=-M_s\Delta^2\sum_{I=2}^{N_z+1}\sum_{J=2}^{N_x+1}H_{0x}\alpha(J,I)+H_{0y}\beta(I,J)+H_{0z}\gamma(J,I)\ , \tag{A26}$$

$$\mathbf{H}_h=\mathbf{x}H_{0x}+\mathbf{y}H_{0y}+\mathbf{z}H_{0z}\ . \tag{A27}$$

[1]F. Bloch, Z. Phys. **74**, 295 (1932).
[2]L. Landau and E. Lifshitz, Phys. Z. Sowjet Union **8**, 153 (1935).
[3]L. Néel, Cah. Phys. **25**, 1 (1944).
[4]L. Néel, Cah. Phys. **25**, 21 (1944).
[5]E. C. Stoner, Phys. Soc. Rep. Prog. Phys. **11**, 43 (1948).
[6]C. Kittel, Rev. Mod. Phys. **21**, 541 (1949).
[7]B. A. Lilley, Philos. Mag. **41**, 792 (1950).
[8]L. Néel, J. Phys. Radiat. **15**, 225 (1954).
[9]S. Middlehoek, J. Appl. Phys. **34**, 1054 (1963).
[10]W. F. Brown and A. E. LaBonte, J. Appl. Phys. **36**, 1380 (1965).
[11]A. E. LaBonte, J. Appl. Phys. **40**, 2450 (1969).
[12]A. Aharoni, J. Appl. Phys. **37**, 3271 (1966).
[13]A. Aharoni, J. Appl. Phys. **38**, 3196 (1967).
[14]A. Aharoni, Philos. Mag. **26**, 1473 (1972).
[15]A. Aharoni, Phys. Status Solidi A **18**, 661 (1973).
[16]A. Aharoni, J. Appl. Phys. **46**, 908 (1975).
[17]A. Aharoni, J. Appl. Phys. **46**, 914 (1975).
[18]A. Hubert, Phys. Status Solidi **32**, 519 (1969).
[19]A. Hubert, Phys. Status Solidi **38**, 699 (1970).
[20]J. P. Jakubovics, Philos. Mag. **30**, 983 (1974).
[21]J. P. Jakubovics, Philos. Mag. B **37**, 761 (1978).
[22]J. P. Jakubovics, Philos. Mag. B **38**, 401 (1978).
[23]H. A. M. van den Berg, J. Appl. Phys. **57**, 2168 (1985).
[24]H. A. M. van den Berg, J. Appl. Phys. **60**, 1104 (1986).
[25]M. E. Schabes and A. Aharoni, IEEE Trans. Magn. **MAG-23**, 3882 (1987).
[26]M. E. Schabes and H. N. Bertram, J. Appl. Phys. **64**, 1347 (1988).
[27]C. C. Shir, J. Appl. Phys. **49**, 3413 (1978).
[28]R. Victora, Phys. Rev. Lett. **58**, 1788 (1987).
[29]R. Victora, J. Appl. Phys. **62**, 4220 (1987).
[30]U. Hartmann, Phys. Status Solidi A **101**, 227 (1987).
[31]U. Hartmann, Phys. Status Solidi A **103**, 247 (1987).
[32]N. Hayashi, T. Inoue, Y. Nakatani, and H. Fukushima, IEEE Trans. Magn. **MAG-24**, 3111 (1988).
[33]H. W. Fuller and M. E. Hale, J. Appl. Phys. **31**, 238 (1960).
[34]T. Suzuki, C. H. Wilts, and C. E. Patton, J. Appl. Phys. **39**, 1983 (1968).
[34]H. Happert and P. Schmiesing, Phys. Status Solidi A **4**, 737 (1971).
[36]C. G. Harrison and K. D. Leaver, Phys. Status Solidi A **12**, 413 (1972).
[37]C. G. Harrison and K. D. Leaver, Phys. Status Solidi A **15**, 415 (1973).
[38]D. C. Hothersall, Phys. Status Solidi B **51**, 529 (1972).
[39]S. Tsukahara and H. Kawakatsu, J. Phys. Soc. Jpn. **32**, 1493 (1972).
[40]T. Suzuki, K. Suzuki, and Y. Igarashi, Jpn. J. Appl. Phys. **15**, 707 (1976).
[41]T. Suzuki and K. Suzuki, IEEE Trans. Magn. **MAG-13**, 1505 (1977).
[42]J. N. Chapman, G. R. Morrison, J. P. Jakubovics, and R. A. Taylor, J. Magn. Magn. Mater. **49**, 277 (1985).
[43]G. R. Morrison, H. Gong, J. N. Chapman, and V. Hrnciar, J. Appl. Phys. **64**, 1338 (1988).
[44]I. R. McFayden, J. Appl. Phys. **64**, 6011 (1988).
[45]K. Tsuno, Rev. Solid State Sci. **2**(4), 623 (1988).
[46]I. Beardsley, IEEE Trans. Magn. **MAG-25**, 671 (1989).
[47]F. Schmidt, W. Rave, and A. Hubert, IEEE Trans. Magn. **MAG-21**, 1596 (1985).
[48]D. A. Herman, B. E. Argyle, and B. Petek, J. Appl. Phys. **61**, 4200 (1987).
[49]P. Ryan and T. B. Mitchell, J. Appl. Phys. **63**, 3162 (1988).
[50]A. L. Olson, H. N. Oredson, E. J. Torok, and R. A. Spurrier, J. Appl. Phys. **38**, 1349 (1967).
[51]U. Hartmann and H. H. Mende, J. Phys. D **18**, 2285 (1985).
[52]U. Hartmann, J. Magn. Magn. Mater. **68**, 298 (1987).
[53]H. P. Oepen and J. Kirschner, Phys. Rev. Lett. **62**, 819 (1989).
[54]M. R. Scheinfein, J. Unguris, R. J. Celotta, and D. T. Pierce, Phys. Rev. Lett. **63**, 668 (1989).
[55]D. T. Pierce, R. J. Celotta, J. Unguris, and H. C. Siegmann, Phys. Rev. B **26**, 2566 (1982).
[56]D. Muari, D. Scholl, H. C. Siegmann, and E. Kay, Phys. Rev. Lett. **61**, 758 (1988).
[57]J. Mathon and S. B. Ahmad, Phys. Rev. B **37**, 660 (1988).
[58]J. Mathon, Physica B **149**, 31 (1988).
[59]R. Allenspach, M. Taborelli, M. Landolt, and H. C. Siegmann, Phys. Rev. Lett. **56**, 953 (1986).
[60]A. J. Freeman and C. L. Fu, J. Appl Phys. **61**, 2256 (1987).
[61]C. H. Smith, J. Appl. Phys. **64**, 6032 (1988).
[62]G. G. Hembree, J. Unguris, R. J. Celotta, and D. T. Pierce, Scanning Microsc. Int. Suppl. **1**, 229 (1987).
[63]K. Koike, H. Matsutama, and K. Hayakawa, Scanning Microsc. Int. Suppl. **1**, 241 (1987).
[64]T. VanZandt, R. Browning, C. R. Helms, H. Poppa, and M. Landolt, Rev. Sci. Instrum. **60**, 3430 (1989).
[65]J. Unguris, D. T. Pierce, and R. J. Celotta, Rev. Sci. Instrum. **57**, 1314 (1986).
[66]M. R. Scheinfein, D. T. Pierce, J. Unguris, J. J. McClellend, and R. J. Celotta, Rev. Sci. Instrum. **60**, 1 (1989).
[67]M. R. Scheinfein, J. Unguris, M. H. Kelley, D. T. Pierce, and R. J. Celotta, Rev. Sci. Instrum. **61**, 2501 (1990).
[68]J. Unguris, M. R. Scheinfein, R. J. Celotta, and D. T. Pierce, in *Chemistry and Physics of Solid Surfaces VII,* edited by R. Vaneslow and R. Howe (Springer-Verlag, Berlin, 1990).
[69]F. R. N. Nabarro, J. Phys. **33**, 1089 (1972).
[70]M. R. Scheinfein, J. Unguris, D. T. Pierce, and R. J. Celotta, J. Appl. Phys. **67**, 5932 (1990).
[71]D. E. Newbury, D. E. Joy, P. Echlin, C. E. Fiori, and J. I. Goldstein, *Advanced Scanning Electron Microscopy and X-Ray Microanalysis* (Plenum, New York, 1986).
[72]H. Seiler, J. Appl. Phys. **54**, R1 (1983).
[73]M. B. Wilk and R. Gnanadesikan, Biometrika **36**, 293 (1968).
[74]G. T. Rado and J. R. Weertman, J. Phys. Chem. Solids **11**, 315 (1959).
[75]G. R. Rado, Phys. Rev. B **40**, 407 (1989).
[76]C. Herring and C. Kittel, Phys. Rev. **81**, 869 (1951).

[77]G. Shirane, V. J. Minkiewicz, and R. Nathans, J. Appl. Phys. **39**, 383 (1968).
[78]B. D. Cullity, *Introduction To Magnetic Materials* (Addison-Wesley, Reading, MA, 1972).
[79]G. T. Rado, Phys. Rev. B **26**, 295 (1982).
[80]G. A. Prinz, G. T. Rado, and J. J. Krebs, J. Appl. Phys. **53**, 2087 (1982).
[81]M. Sparks, *Ferromagnetic Relaxation Theory* (McGraw-Hill, New York, 1964).
[82]A. P. Malozemoff and J. C. Slonczewski, *Magnetic Domain Walls In Bubble Materials* (Academic, New York, 1979).
[83]M. R. Scheinfein and J. L. Blue, J. Appl. Phys. (to be published).
[84]N. Smith, D. Markham, and D. LaTourette, J. Appl. Phys. **65**, 4362 (1989).
[85]S. Chikazumi, *Physics of Magnetism* (Wiley, New York, 1964).
[86]The Fe wiskers were furnished by A. Arrott.
[87]N. Draper and H. Smith, *Applied Regression Analysis* (Wiley, New York, 1966).
[88]B. Efron, *The Jacknife, the Bootstrap and Other Resampling Plans* (Society for Industrial and Applied Mathematics, Philadelphia, PA, 1982).
[89]H. Hoffmann, IEEE Trans. Magn. **MAG-4**, 32 (1968).
[90]M. R. Scheinfein, P. Ryan, J. Unguris, D. T. Pierce, and R. J. Celotta, Appl. Phys. Lett. **57**, 1817 (1990).

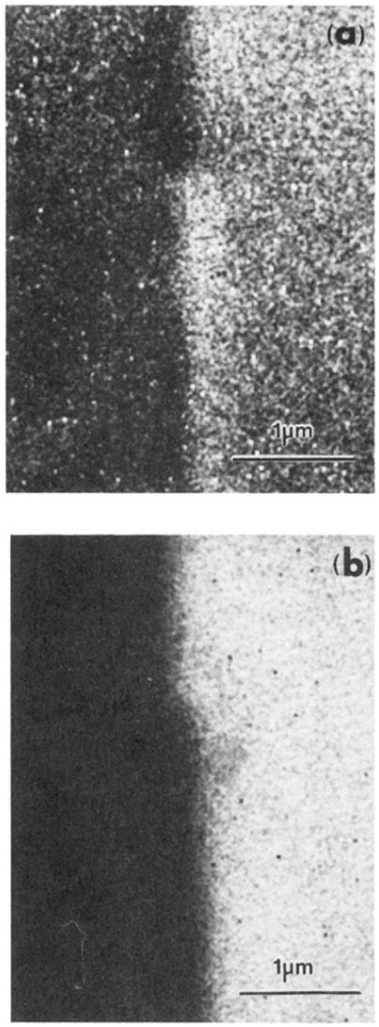

FIG. 2. (a) M_x and (b) M_y SEMPA images from the surface of a single crystal of Fe(100). The surface domain wall runs vertically through the image. In the center is a surface magnetic singularity about which the magnetization circulates.